

Review

# Neutrinoless Double Beta Decay with Germanium Detectors: $10^{26}$ yr and Beyond

Valerio D'Andrea <sup>1,2</sup> , Natalia Di Marco <sup>2,3,\*</sup> , Matthias Bernhard Junker <sup>2</sup> , Matthias Laubenstein <sup>2</sup> ,  
Carla Macolino <sup>1,2</sup> , Michele Morella <sup>2,3</sup> , Francesco Salamida <sup>1,2</sup>  and Chiara Vignoli <sup>2</sup> 

- <sup>1</sup> Dipartimento di Scienze Fisiche e Chimiche, Università degli Studi dell'Aquila, 67100 L'Aquila, Italy; valerio.dandrea@lngs.infn.it (V.D.); carla.macolino@univaq.it (C.M.); francesco.salamida@aquila.infn.it (F.S.)
- <sup>2</sup> INFN—Laboratori Nazionali del Gran Sasso, Assergi, 67100 L'Aquila, Italy; matthias.junker@lngs.infn.it (M.B.J.); matthias.laubenstein@lngs.infn.it (M.L.); michele.morella@gssi.it (M.M.); chiara.vignoli@lngs.infn.it (C.V.)
- <sup>3</sup> Gran Sasso Science Institute, 67100 L'Aquila, Italy
- \* Correspondence: natalia.dimarco@gssi.it

**Abstract:** In the global landscape of neutrinoless double beta ( $0\nu\beta\beta$ ) decay search, the use of semiconductor germanium detectors provides many advantages. The excellent energy resolution, the negligible intrinsic radioactive contamination, the possibility of enriching the crystals up to 88% in the  $^{76}\text{Ge}$  isotope as well as the high detection efficiency, are all key ingredients for highly sensitive  $0\nu\beta\beta$  decay search. The MAJORANA and GERDA experiments successfully implemented the use of germanium (Ge) semiconductor detectors, reaching an energy resolution of  $2.53 \pm 0.08$  keV at the  $Q_{\beta\beta}$  and an unprecedented low background level of  $5.2 \times 10^{-4}$  cts/(keV·kg·yr), respectively. In this paper, we will review the path of  $0\nu\beta\beta$  decay search with Ge detectors from the original idea of E. Fiorini et al. in 1967, to the final recent results of the GERDA experiment setting a limit on the half-life of  $^{76}\text{Ge}$   $0\nu\beta\beta$  decay at  $T_{1/2} > 1.8 \times 10^{26}$  yr (90% C.L.). We will then present the LEGEND project designed to reach a sensitivity to the half-life up to  $10^{28}$  yr and beyond, opening the way to the exploration of the normal ordering region.

**Keywords:** germanium detector; neutrino; neutrinoless double beta decay



**Citation:** D'Andrea, V.; Di Marco, N.; Junker, M.B.; Laubenstein, M.; Macolino, C.; Morella, M.; Salamida, F.; Vignoli, C. Neutrinoless Double Beta Decay with Germanium Detectors:  $10^{26}$  yr and Beyond. *Universe* **2021**, *7*, 341. <https://doi.org/10.3390/universe7090341>

Academic Editors: Fabio Bellini and Claudia Tomei

Received: 15 June 2021  
Accepted: 2 August 2021  
Published: 10 September 2021

**Publisher's Note:** MDPI stays neutral with regard to jurisdictional claims in published maps and institutional affiliations.



**Copyright:** © 2021 by the authors. Licensee MDPI, Basel, Switzerland. This article is an open access article distributed under the terms and conditions of the Creative Commons Attribution (CC BY) license (<https://creativecommons.org/licenses/by/4.0/>).

## 1. Introduction

The evidence for non-zero neutrino masses as a consequence of the neutrino oscillation discovery [1–4] provides, among others, a hint of physics beyond the Standard Model (SM). Despite many experimental efforts carried out about neutrino physics since the first pioneering experiment by Reines and Cowan in 1956 [5], there are still open points to be clarified such as the neutrino nature, the mass ordering and the absolute mass scale.

The search for neutrinoless double beta ( $0\nu\beta\beta$ ) decay is considered as the most promising way to prove the Majorana nature of neutrinos as well as to give an indication on the mass hierarchy and on the absolute mass scale. Moreover, the discovery of  $0\nu\beta\beta$  decay would open the way for theories predicting the observed matter anti-matter asymmetry of the Universe being a consequence of lepton number violation through leptogenesis.

The important implications for particle physics and cosmology justify the experimental efforts carried out worldwide in the field of  $0\nu\beta\beta$  decay searches. A number of different experiments exploiting various technologies and searching for the transition in different isotopes exists:  $^{76}\text{Ge}$  [6,7],  $^{82}\text{Se}$  [8],  $^{100}\text{Mo}$  [9–11],  $^{130}\text{Te}$  [12,13],  $^{136}\text{Xe}$  [14–16] and others.

In this paper, we will review the story of the  $0\nu\beta\beta$  decay search of  $^{76}\text{Ge}$  with germanium semiconductor detectors. The paper is organized as follows. In the second section, a review of the main aspects of the  $0\nu\beta\beta$  theory will be presented. In the third section, we will discuss the choice of the  $^{76}\text{Ge}$  isotope, highlighting the main advantages and disadvantages with respect to other techniques and isotopes. In the fourth section, we will report about

the historical path of  $0\nu\beta\beta$  decay search with germanium detectors from the original idea proposed by E. Fiorini et al. in 1967 [17] to the experiments inaugurating the modern era of highly sensitive, low background searches. In the fifth and sixth section, we will summarize the main characteristics, performance and results of the contemporary GERDA and MAJORANA experiments currently leading the field with the best sensitivity, the lowest background level and the best resolution among all the other  $0\nu\beta\beta$  decay experiments. Finally, in the seventh section, we will present the LEGEND project conceived to extend the sensitivity up to  $10^{28}$  yr to fully cover the inverted hierarchy region.

### 2. Neutrinoless Double Beta Decay

The double beta decay ( $2\nu\beta\beta$ ), first proposed by M. Goeppert-Mayer in 1935 [18], is a second-order process generated in the perturbative expansion of weak interactions in the SM with an extremely long lifetime corresponding to a transition from a nucleus  $(A, Z)$  to  $(A, Z + 2)$ . Candidate isotopes that can decay through the double beta decay are even–even nuclei and lighter than the odd–odd  $(A, Z + 1)$  nucleus, for which the single  $\beta$  decay is forbidden or strongly suppressed because of a large change of spin. In  $2\nu\beta\beta$  decay, starting from the initial nuclear state, one nucleon type (proton or neutron) decays into another one emitting a lepton–anti-lepton pair through a virtual transition, and a second decay occurs producing a further pair of lepton and anti-lepton. The SM, therefore, predicts the emission in the final state of two electrons and two anti-neutrinos:

$$(Z, A) \rightarrow (Z + 2, A) + 2e + 2\bar{\nu} + Q_{\beta\beta}$$

where  $Q_{\beta\beta}$  is the energy released in the decay. The Feynman diagram of this process is shown in the left panel of Figure 1. Among the 35 naturally occurring isotopes that can decay through  $2\nu\beta\beta$ , Table 1 reports the results for the measurement of a few isotopes together with the main characteristics of the process.

The  $0\nu\beta\beta$  decay process, proposed by W.H. Furry in 1939 [19], is a SM-forbidden transition in which the final state consists of only two electrons:

$$(Z, A) \rightarrow (Z + 2, A) + 2e + Q_{\beta\beta}$$

This decay clearly violates the leptonic number conservation ( $\Delta L = 2$ ). The relevant diagram, due to the exchange of light Majorana neutrino, is shown in Figure 1 on the right panel. There are other possible mediators of this decay, e.g., right-handed weak currents, supersymmetric particles and massive neutrinos. Regardless of the underlying mechanisms, the observation of the  $0\nu\beta\beta$  decay would prove that the lepton number conservation is not an exact symmetry of nature and that neutrinos have a Majorana mass component.

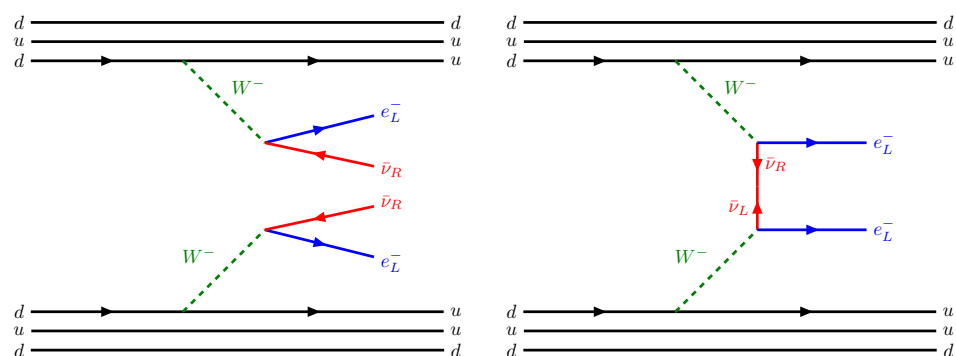


**Figure 1.** On the left, the diagram of the standard  $2\nu\beta\beta$  decay with the emission of 2 anti-neutrinos. On the right, the  $0\nu\beta\beta$  process due to the exchange of a light Majorana neutrino with lepton number violation.

**Table 1.** A list of isotopes mostly used in  $2\nu\beta\beta$  decay experiments. Some of the key features are reported. Half-life values are from [20].

Isotope	Natural Abundance (%)	$Q_{\beta\beta}$ (MeV)	$T_{1/2}^{2\nu}$ (yr)
$^{48}\text{Ca}$	0.187	4.263	$5.3_{-0.8}^{+1.2} \times 10^{19}$
$^{76}\text{Ge}$	7.8	2.039	$(1.88 \pm 0.08) \times 10^{21}$
$^{82}\text{Se}$	9.2	2.998	$0.87_{-0.01}^{+0.02} \times 10^{20}$
$^{96}\text{Zr}$	2.8	3.348	$(2.3 \pm 0.2) \times 10^{19}$
$^{100}\text{Mo}$	9.6	3.035	$7.06_{-0.13}^{+0.15} \times 10^{18}$
$^{116}\text{Cd}$	7.6	2.813	$(2.69 \pm 0.09) \times 10^{19}$
$^{130}\text{Te}$	34.08	2.527	$(7.91 \pm 0.21) \times 10^{20}$
$^{136}\text{Xe}$	8.9	2.459	$(2.18 \pm 0.05) \times 10^{21}$
$^{150}\text{Nd}$	5.6	3.371	$(9.34 \pm 0.65) \times 10^{18}$

In the low energy limit, the interaction of neutrinos can be described by the current-current four-fermion interactions. In this approximation, the half-life of the  $0\nu\beta\beta$  decays can be derived as described in [21]:

$$\left(T_{1/2}^{0\nu}\right)^{-1} = G_{0\nu} \times |M_{0\nu}|^2 \times \left(\frac{m_{\beta\beta}}{m_e}\right)^2 \quad (1)$$

where  $G_{0\nu}$  is the phase space factor (PSF),  $M_{0\nu}$  is the nuclear matrix element (NME) and  $m_{\beta\beta}$  is the effective Majorana mass defined by:

$$m_{\beta\beta} = \sum_{i=1}^3 U_{ei}^2 m_i \quad (2)$$

where  $U$  is the PNMS mixing matrix and  $m_i$  are the neutrino mass eigenvalues. It follows that the decay rate is proportional to  $m_{\beta\beta}^2$  and so the neutrino mass can be estimated from the measurement of the half-life of the  $0\nu\beta\beta$  decay.

The main source of uncertainty in the expected value of the  $0\nu\beta\beta$  decay half-life originates from the NME calculations. They involve the hadronic current of the weak Hamiltonian and depend on the nuclear-structure of the parent and daughter nuclei. They are usually difficult to calculate even in the case of single  $\beta$  decay. Different models are available to calculate the NMEs, e.g., the Interactive Shell Model (ISM) [22], the Quasi-particle Random Phase Approximation (QRPA) [23] and the Interactive Boson Model (IBM-2) [24]. A comparison between the values of the NMEs calculated with the different models is illustrated in Figure 2. Despite the fact that the uncertainty on the single calculation is of the order of 20%, the differences between the different models are even larger. The overall estimate of the NME calculation is therefore affected by a large systematic uncertainty.

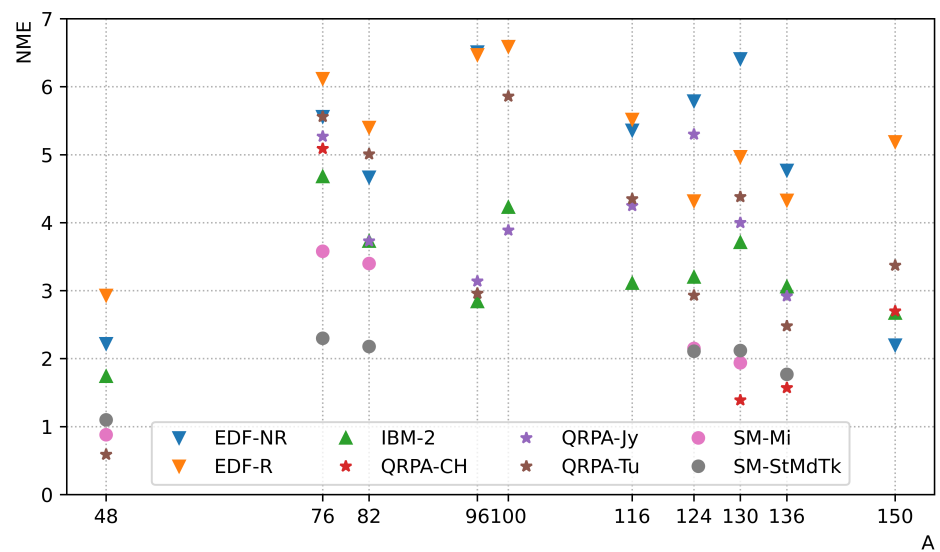


**Figure 2.** Comparison of NME calculations with an unquenched  $g_A = 1.27$  for different isotopes and with various models. Abbreviations: EDF, energy-density functional; IBM, interacting boson model; NME, nuclear matrix element; QRPA, quasi-particle random-phase approximation; SM, Standard Model. The reader should refer to [25] for further details.

Parametrizing the NME as in [26], we can write:

$$M_{0\nu} = g_A^2 \left( M_{GT}^{0\nu} - \left( \frac{g_V}{g_A} \right)^2 M_F^{0\nu} + M_T^{0\nu} \right) \tag{3}$$

where  $g_V$  and  $g_A$  are the vector and axial coupling constants of the nucleon,  $M_{GT}^{0\nu}$  is the Gamow–Teller operator matrix element between the initial and the final states,  $M_F^{0\nu}$  is the Fermi contribution and  $M_T^{0\nu}$  is the tensor operator matrix element. Equation (3) emphasizes the role of  $g_A$  being  $T_{1/2}^{0\nu}$  proportional to  $g_A^{-4}$ . The value of  $g_A$  can be used as an adjustment to reconcile observations with calculations. In the hypothesis of quenching, a reduction of  $g_A$  is assumed to reproduce the observable quantities of  $\beta$  and  $2\nu\beta\beta$  decays [27]. There are different possible origins for quenching, e.g., many-body currents, intrinsic shortcomings of the nuclear many-body models, or nuclear medium effects [25]. Recent studies point towards quenching not being larger than 20–30% in processes with high momentum transfer such as the  $0\nu\beta\beta$  decay. This reduction would result in an increase of  $T_{1/2}^{0\nu}$  by a factor of two or three.

### 3. The Choice of the $^{76}\text{Ge}$ Isotope

From the experimental point of view, the search for  $0\nu\beta\beta$  decay consists of the detection of the two emitted electrons. As the recoil of the nucleus negligible, the sum of energies of the two electrons corresponds to the Q-value of the process. The signature of the  $0\nu\beta\beta$  decay is therefore a mono-energetic peak centered at  $Q_{\beta\beta}$  (see Figure 3).

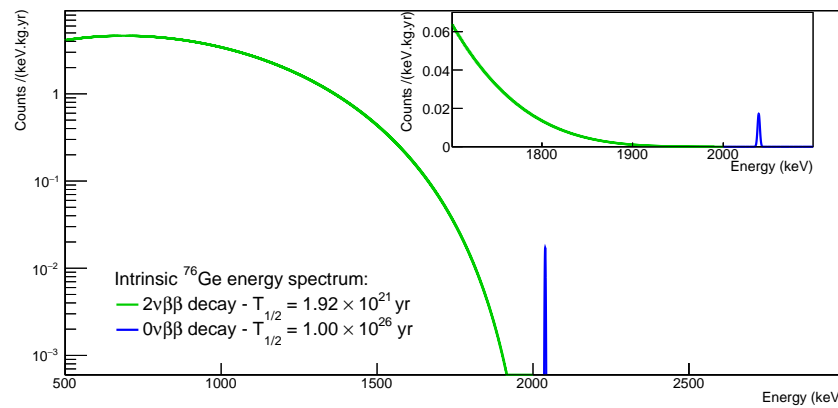


Figure 3. Schematic view of the expected  $0\nu\beta\beta$  and  $2\nu\beta\beta$  decay spectra. Credits to GERDA Collaboration.

Since the value of  $Q_{\beta\beta}$  is well known, the search for a  $0\nu\beta\beta$  decay signal can be performed in a very narrow region of interest (ROI). The number of signal events expected in the ROI is given by:

$$N^{0\nu} = \ln(2) \frac{N_A}{m_A} \left( \frac{M T \varepsilon a}{T_{1/2}^{0\nu}} \right) \tag{4}$$

where  $N_A$  is the Avogadro constant,  $m_A$  and  $a$  are the molar mass and the isotopic abundance of the double beta ( $\beta\beta$ ) emitter, respectively,  $\varepsilon$  is the detection efficiency,  $M$  is the detector mass and  $T$  is the measurement time of the experiment. On the other hand, the number of background events in the ROI is given by:

$$N_b = BI M T \Delta E \tag{5}$$

where  $\Delta E$  is the ROI width, proportional to the energy resolution of the detector, and BI is the background index, normalized to the width of the ROI, mass, energy and time and expressed in units of  $\text{keV}^{-1} \cdot \text{kg}^{-1} \cdot \text{year}^{-1}$ . The sensitivity of the experiment can be obtained requiring that the  $0\nu\beta\beta$  decay signal exceeds the standard deviation of the total detector counts  $N^{0\nu} \geq n_\sigma \sqrt{N^{0\nu} + N_b}$  where  $n_\sigma$  is the confidence level expressed in units of  $\sigma$ s of the Poisson distribution. Combining Equations (4) and (5), the sensitivity can be derived as:

$$S^{0\nu} = \ln(2) \frac{N_A}{m_A} \left( \frac{\varepsilon a}{n_\sigma} \right) \sqrt{\frac{M T}{BI \Delta E}} \tag{6}$$

This formula clearly shows the role of the different experimental parameters and highlights the different characteristics that have to be chosen to improve the  $0\nu\beta\beta$  decay discovery probability. In particular, the ideal experiment should have an isotope with high isotopic abundance  $a$ , a high detection efficiency  $\varepsilon$ , the possibility to deploy a large amount of mass, a low background and a good energy resolution.

Among  $\beta\beta$ -emitters,  $^{130}\text{Te}$  has the highest isotopic abundance and a tellurium-based experiment does not necessarily require enrichment. Tellurium dioxide crystals ( $^{nat}\text{TeO}_2$ ), as the ones employed in CUORE [12], are used as cryogenic calorimeters detecting the small temperature rise induced by the energy deposition of a charged particle. As in all experiments where the source of  $0\nu\beta\beta$ -decay events coincides with the detector, the detection efficiency is maximized. Although reaching a very good energy resolution ( $\sim 0.3\%$  FWHM at  $Q_{\beta\beta}$ , second only to germanium diodes), phonon detection only does not allow to perform particle identification to reject background events. This leads to a higher background index and prevents entering the background-free regime. Moreover, the  $Q_{\beta\beta}$  of  $^{130}\text{Te}$  (see Table 1) is lower than the  $^{208}\text{Tl}$  gamma line at 2.6 MeV, which therefore contributes to the background around  $Q_{\beta\beta}$ . The solution to overcome this limitation is the use of scintillating bolometers employing different isotopes, namely  $\text{Zn}^{82}\text{Se}$  for CUPID-0 [8] and  $\text{Li}^{100}\text{MoO}_4$  for CUPID-Mo [11]. Both of these isotopes have a  $Q_{\beta\beta}$  around 3 MeV, above the  $^{208}\text{Tl}$  line

and most of the other natural radioactive background sources, but very low natural isotopic abundance (in this case, enrichment is required).  $\text{Li}^{100}\text{MoO}_4$  crystals will be the ones implemented in the final version of the next generation ton-scale experiment CUPID [28]. This is mainly due to the poor radiopurity and energy resolution of  $\text{Zn}^{82}\text{Se}$  produced, even though  $^{100}\text{Mo}$   $2\nu\beta\beta$  decay half-life (the fastest among the ones in Table 1) could be an irreducible source of background around  $Q_{\beta\beta}$  if energy and time resolution requirements will not be satisfied.

Although having a  $Q_{\beta\beta}$  below  $^{208}\text{Tl}$ ,  $^{136}\text{Xe}$  is an interesting candidate isotope as it is gaseous, easy to enrich and can be used to build a ton-scale experiment. Also in this case, the detector itself is the source of  $0\nu\beta\beta$ -decay, and different technologies can be implemented: a single phase Time Projection Chamber (TPC) using Liquid Xenon (LXe), such as EXO-200 [29], a high-pressure TPC with Gaseous Xenon (GXe), such as NEXT [30], or a Xe-loaded liquid scintillator, such as KamLAND-Zen [31]. The achievable energy resolution is lower with respect to germanium or bolometric experiments and it ranges roughly from 1% to 10% FWHM among different experiments. LXe-TPCs measure both the scintillation light (starting time for the TPC) and ionization charges and have a better self-shielding against external background sources (due to the higher density of the target). Furthermore, some topological information to distinguish single site from multi site events was used in EXO-200 [29]. GXe-TPCs allow for real topological reconstruction: because of the lower density of the detector, a  $0\nu\beta\beta$  event would look like two separate tracks (originating from the same point, the decaying nucleus) ending with Bragg peaks, corresponding to the stopping of the two emitted electrons. In this way, it is possible to reject nearly any possible background event except  $2\nu\beta\beta$ . Xe-based experiments did not reach a background-free regime up to now; thus, the  $0\nu\beta\beta$  decay (and also any other physics) search heavily depends on the background model of the experiment.

Germanium detectors are particularly suited for  $0\nu\beta\beta$  decay search, presenting indeed several advantages. As the search for  $0\nu\beta\beta$  decay is based on the detection of a signal peak over the background, the excellent energy resolution of semiconductor detectors results in a great advantage. High Purity Germanium (HPGe) detectors have the best energy resolution with respect to any other competitive technique with a full width at half maximum (FWHM) better than 0.1% at the  $Q$ -value of the  $0\nu\beta\beta$  decay of  $^{76}\text{Ge}$  ( $Q_{\beta\beta} = 2039$  keV) (see Sections 5 and 6). This feature allows to identify the  $\gamma$  peaks of the various background sources as well as to isolate the tail of the  $2\nu\beta\beta$  decay spectrum (see Figure 3). Germanium-based experiments feature a high detection efficiency since the detector is also the source of the  $\beta\beta$ -decay. Despite the relatively low natural isotopic abundance of the germanium  $\beta\beta$ -emitter  $^{76}\text{Ge}$  (7.8%), modern experiments make use of crystals enriched in  $^{76}\text{Ge}$  ( $^{\text{enr}}\text{Ge}$ ) up to 88%, thus significantly reducing the number of detectors needed to reach a given  $^{76}\text{Ge}$  content. HPGe detectors also guarantee a low background level since they have an extremely high intrinsic radio-purity (no measurable U or Th contamination) and can be realized with particular electrode geometry, allowing to take advantage of the pulse shape discrimination (PSD) analysis to actively reduce the background (see Sections 5 and 6).

On the other hand, the use of germanium presents a few disadvantages. The  $Q_{\beta\beta}$  of  $^{76}\text{Ge}$  is low with respect to other commonly used  $\beta\beta$  isotopes. In particular, the  $Q_{\beta\beta}$  is below the dominant  $^{208}\text{Tl}$  line of 2615 keV, thus causing the ROI suffering of the relative Compton continuum. The enrichment process is a rather expensive procedure even if the cost has been decreasing through the years. Although taking advantage from a high value of  $M_{0\nu}$ ,  $^{76}\text{Ge}$  has the lowest value of the space phase factor ( $\sim 2.3 \times 10^{-15}$  [32,33]) with respect to all other isotopes. This implies the need to reach a longer  $T_{1/2}^{0\nu}$  to probe a given  $m_{\beta\beta}$  value.

Modern experiments using HPGe detectors have already faced the listed issues and are currently leading the field with the best limit and the best sensitivity on the  $0\nu\beta\beta$  decay half-life with the GERDA experiment (see Section 5), thus approaching the exploration of the inverted ordering region. PSD techniques and additional active veto systems have been successfully exploited to get rid of  $\gamma$  background and other residual contamination. These

factors, together with a careful material selection, led GERDA to achieve an unprecedented low background level thus, reaching the so-called background-free regime (see Section 5).

#### 4. Neutrinoless Double Beta Decay Search with Ge Detectors

The observation of the  $\beta\beta$ -decay can be performed through geochemical, radiochemical and direct techniques. In the geochemical method [34], the abundance of the daughter isotope is determined in minerals of known age containing the parent nucleus. In the radiochemical method, the abundance of the final nucleus is measured after several years in a well-prepared artificial sample of the parent one. In both methods, however,  $0\nu\beta\beta$  and  $2\nu\beta\beta$  decays cannot be distinguished, while in direct experiments, the measurement of the sum energy of the two emitted electrons provides a real-time detection of the  $\beta\beta$ -decay.

The search for  $0\nu\beta\beta$  decay with Ge detectors was firstly proposed in 1967 by the Milano Group [17] using a Ge(Li) detector [35,36]. The experiment was located in the Mont Blanc tunnel ( $\sim 4200$  m.w.e.) in order to reduce cosmic-ray background. The 90 g Ge detector was surrounded by a plastic scintillator veto and shielded with 10 cm of low background lead, a thin cadmium neutron absorbing layer and a 10 cm-thick box of resin impregnated wood as a neutron moderator. The outer shield was 10 cm-thick ordinary lead [37]. In the following years, the Milano group upgraded the experiment with two true coaxial Ge(Li) detectors and made several improvements regarding the use of low-background construction materials for the cryostat and a new shielding configuration [38,39]. No evidence for  $0\nu\beta\beta$  decay of  $^{76}\text{Ge}$  was found, and a lower limit on the half-life of  $3.3 \times 10^{23}$  yr (68% C.L.) was set in 1986 [39].

In the 1970s and 1980s, several research groups started to search for the  $0\nu\beta\beta$  decay of  $^{76}\text{Ge}$  with HPGe detectors, making strong efforts to reduce the background through the use of passive shields, by placing the experiments in underground facilities [40–43] and by using an active NaI veto [44–48]. The strongest limit on the  $0\nu\beta\beta$  decay half-life reported by a natural Ge experiment was  $1.2 \times 10^{24}$  yr (UCSB/LBL [48]).

For the first time, the ITEP-Yerevan experiment [49] employed Ge(Li) detectors isotopically enriched in  $^{76}\text{Ge}$  in order to concentrate the active source mass in small detectors and set a limit of  $T_{1/2}^{0\nu} \geq 2.0 \times 10^{24}$  yr in 1989.

Following this idea, in the 1990s, two collaborations produced the first  $^{\text{enr}}\text{Ge}$  HPGe detectors: the Heidelberg–Moscow (HDM) experiment [50–54] and the International Germanium Experiment (IGEX) [55,56]. The HDM experiment operated 16.9 kg of  $^{\text{enr}}\text{Ge}$  with a  $^{76}\text{Ge}$  abundance of 86% at the LNGS. The IGEX collaboration produced six  $^{\text{enr}}\text{Ge}$  detectors that were operated in a low-background cryostat with archaeological lead shielding in different underground facilities. Both HDM and IGEX experiments applied pulse shape discrimination (PSD) analysis to further reduce the background. A lower limit on the half-life of the decay of  $1.9 \times 10^{25}$  yr (90% C.L.) was found by the HDM collaboration [53].

In 2001, after the publication of the final results of HDM part of the collaboration published a claim on the observation of the  $0\nu\beta\beta$  decay of  $^{76}\text{Ge}$  [57], reporting a half-life of  $T_{1/2}^{0\nu} = 1.19_{-0.23}^{+0.37} \times 10^{25}$  yr [58]. Later, pulse shape discrimination was used to strengthen the claim [59]. This claim arose a number of replies and was strongly criticized by many physicists [60]. The situation was clarified only a few years later by the results from the first phase of the GERDA experiment [61] that strongly disfavored the observation.

The GERDA [6,61–64] and MAJORANA [7,65] experiments continued the search for the  $^{76}\text{Ge}$   $0\nu\beta\beta$  decay with Ge detectors in the last decade, reaching a sensitivity larger than  $10^{26}$  yr. Details on these experiments are presented in Sections 5 and 6.

The evolution of the published results on the lower limit of the half-life of  $^{76}\text{Ge}$   $0\nu\beta\beta$  decay is depicted in Figure 4, from the first result of the Milano group [17] until the final result of the GERDA experiment [64].

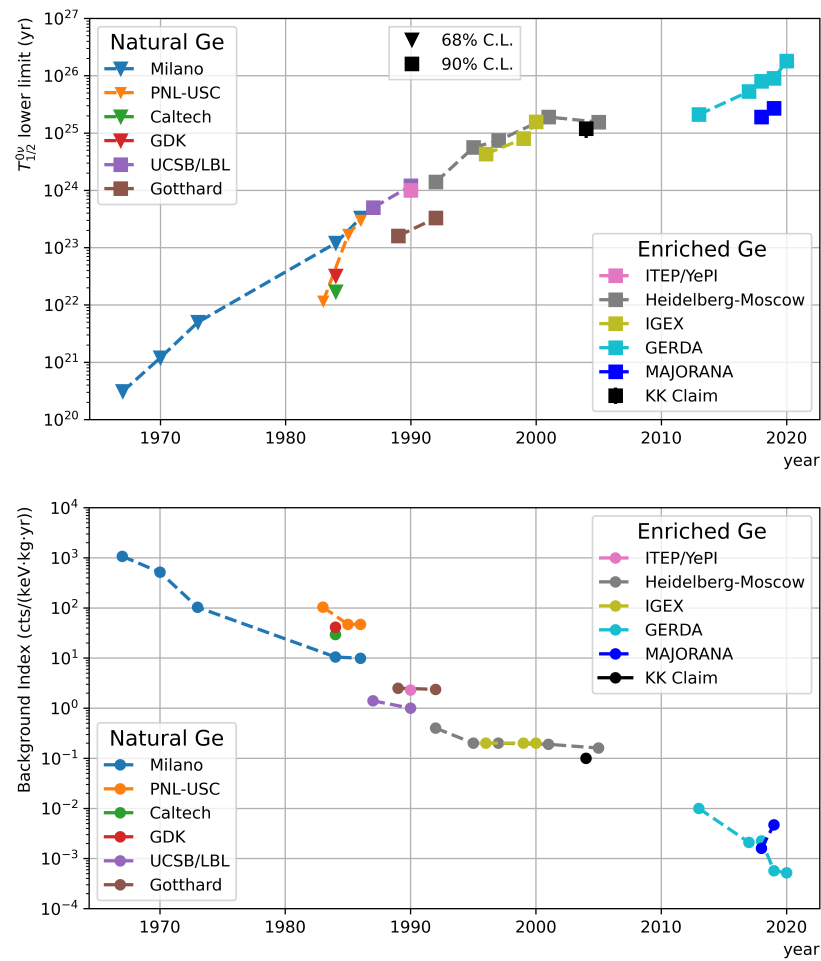


**Figure 4.** Evolution of the lower limit on the half-life (**upper** panel) and background index (**bottom** panel) as a function of time for the experiments searching for  $^{76}\text{Ge}$   $0\nu\beta\beta$  decay. References are in the text (see Section 4).

The intense experimental program and the technology progress allowed tightening the limit of six orders of magnitude in about 50 years. This goal has been achieved thanks to the excellent performance of the Ge detectors and the possibility of operating an increasing  $^{76}\text{Ge}$  mass, together with the impressive improvement in the background reduction techniques (e.g., strong material selection, introduction of active vetoes and efficient pulse shape discrimination analysis). Figure 4 (bottom) reports the evolution in time of the background index of germanium experiments: the BI was progressively decreasing as the sensitivity increased until reaching the background-free regime with the GERDA experiment [62].

The search for  $0\nu\beta\beta$  decay in  $^{76}\text{Ge}$  will be continued in the following years by the LEGEND project [66]: with a staged approach, it aims to reach a sensitivity to the  $0\nu\beta\beta$  decay half-life up to  $10^{28}$  yr. The experimental program of LEGEND is described in Section 7.

### 5. The GERDA Experiment

The experimental apparatus of the GERmanium Detector Array (GERDA) experiment is installed in hall A of the Gran Sasso National Laboratory (LNGS). The experiment was taking data from 2011 to 2019 through different phases. The facility is currently being upgraded to host the first phase of the LEGEND project, called LEGEND-200 (see Section 7).

The core of the GERDA experiment was made of HPGe detectors isotopically enriched in  $^{76}\text{Ge}$  up to  $\sim 87\%$  [67,68]. Following a suggestion from [69], the detectors were directly immersed into liquid Argon (LAr), which acts both as a shield against the external radioac-

tivity and as a cooling medium. In the different phases of the experiment, the germanium mass was progressively increased using different types of detectors.

In GERDA Phase I, lasting from November 2011 to September 2013 and collecting an exposure of 23.5 kg·yr, eight enriched semi-coaxial Ge detectors (see Figure 5a), for a total mass of 15.6 kg, were employed together with three non-enriched semi-coaxial detectors. The semi-coaxial detectors were originally produced by ORTEC for the former HDM [53] and IGEX [56] experiments (see Section 4), then refurbished by Canberra and redeployed in the GERDA apparatus. In July 2012, the natural Ge detectors were replaced by five Broad Energy Germanium (BEGe) diodes [70] (see Figure 5b) with a total mass of 3.6 kg. The detectors were arranged in four strings, each one housing three (five) semi-coaxial (BEGe) detectors.

From September 2013 to December 2015, a major upgrade of the experiment was carried out to improve the sensitivity to the  $0\nu\beta\beta$  decay half-life of  $^{76}\text{Ge}$  beyond  $10^{26}$  yr with a goal exposure of 100 kg·yr [68]. The GERDA Phase II was designed to reach a BI of the order of  $10^{-3}$  cts/(keV·kg·yr), thus running in the so-called background-free regime, i.e., having less than one background event in the energy region ( $Q_{\beta\beta} \pm 0.5$  FWHM) for the whole exposure. In the background-free regime, the sensitivity is expected to scale linearly with the exposure, thus allowing to reach the desired final goal. The GERDA Phase II detectors array included 40 diodes in total, composed of 7 Phase I semi-coaxial detectors, 30 newly produced BEGes (for a mass of about 20 kg) and 3 non-enriched semi-coaxial detectors.

The data-taking of GERDA Phase II started in December 2015. From April 2018 to July 2018, after having collected an exposure of 58.9 kg·yr [6], a minor upgrade of the experiment was carried out with the installation of five additional inverted coaxial (IC [71,72]) detectors (see Figure 5c), produced in collaboration with Mirion Technologies with a total mass of 9.6 kg. The data-taking was then resumed and lasted till November 2019 for a final total collected exposure of 103.7 kg·yr [64].

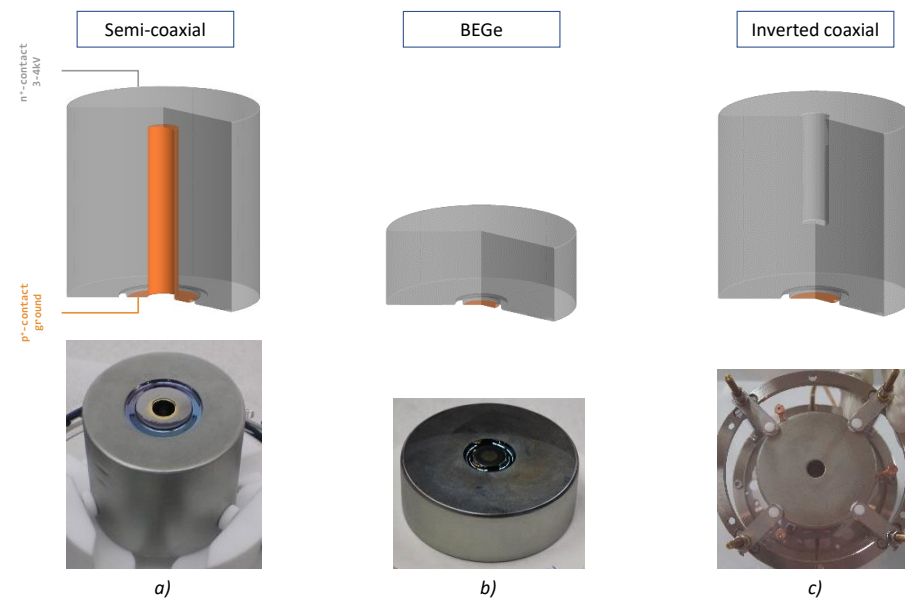


**Figure 5.** Sketch (top) and picture (bottom) of semi-coaxial (a), BEGe (b) and inverted coaxial (c) detectors employed in the various phases of the GERDA experiment.

### 5.1. Experimental Setup

The 3500 m.w.e. of rock overburden of the LNGS site, where the GERDA apparatus is installed, provides a reduction of the cosmic muon flux by six orders of magnitude with respect to surface.

The experimental setup consists of a 590 m<sup>3</sup> stainless steel tank of 9 m height and 10 m diameter, filled with ultra-pure water [67]. The tank is instrumented with 66 photomulti-

pliers tubes (PMTs), acting as an active Cherenkov veto against the residual cosmic muon flux. The muon veto system [73] is complemented by scintillator panels installed on the top of the clean room, as shown in Figure 6.

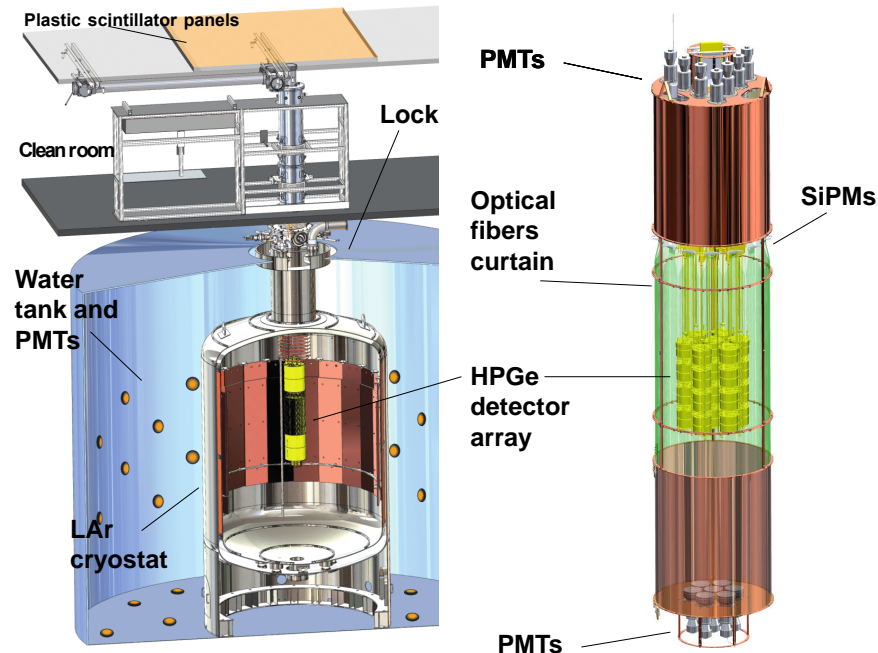


**Figure 6.** Schematic view of the GERDA setup. Figure published by Nature, 2017 [62].

The water tank contains a 64 m<sup>3</sup> vacuum-insulated stainless steel cryostat (diameter = 4 m), filled with LAr. The internal walls of the cryostat are covered with a 6 cm low-background copper (Cu) layer to shield the  $\gamma$  radioactivity originating from the steel.

The 40 germanium detectors employed in GERDA Phase II were arranged in seven strings, each one surrounded by a nylon cylindrical vessel conceived to reduce the collection of <sup>42</sup>K ions, originating from the decay of <sup>42</sup>Ar, onto the surface of the detectors. The array is lowered in the LAr cryostat from the clean room above the tank through the lock system, as shown in Figure 6.

During the upgrade between Phase I and Phase II, a cylindrical volume around the detector string of about 1 m height and 0.5 m diameter was instrumented with a curtain of wavelength-shifting fibers to detect the LAr scintillation light. The readout was performed using 90 silicon photomultipliers (SiPMs) and 16 PMTs, arranged as shown on the right side of Figure 6. Both water and LAr systems act simultaneously as a passive shield from external radioactivity and neutrons and as active vetoes. This setup allows suppressing the external  $\gamma$  background at  $Q_{\beta\beta}$  to less than 10<sup>-5</sup> cts/(keV·kg·yr) [74], while the muon rejection efficiency is >99.9% [73].

While differing in size and geometry (see Figure 5), both semi-coaxials and BEGes are p-type semiconductor detectors operated in reverse bias mode. They are fabricated from high purity Ge crystals with an active net impurity concentration of around 10<sup>10</sup> atoms/cm<sup>3</sup> [6]. The n+ contact is made of diffused lithium with a thickness of about 0.5 mm. The p+ contact is made of ion-implanted boron with a thickness of the order of 100  $\mu$ m. The semi-coaxial diodes have a mass of the order of 2 kg and an enrichment fraction ranging from 85.5 to 88.3% [68]. The BEGes detectors have a diameter ranging from 58.3 to 79.3 mm and heights from 22.9 to 35.3 mm [68], with a mass of the order of O(0.8) kg. The enrichment fraction is 87.8%. IC detectors have a mass of the order of 2 kg, a diameter ranging from 72.6 to 76.6 mm and heights from 80.4 to 85.4 mm. The enrichment fraction is 88% [72].

The different readout electrode layout of semi-coaxial, BEGe and IC is at the basis of their different mass and performance. The geometry of the p+ contact of a coaxial detector

allows the depletion of a larger volume with respect to a BEGe. Conversely, the latter, thanks to its small p+ electrode, features a lower capacitance (1 pF vs. 30 pF), thus resulting in a lower series noise and in a superior energy resolution. This difference is also the key for the better Pulse Shape Discrimination (PSD) performance of BEGe detectors. The new design of IC detectors allows to increase the detector mass to the level of a coaxial diode, thus lowering the background amount per mass unit while retaining the resolution and the PSD performance of BEGes (see Section 5.2).

The readout of germanium detectors is performed using charge sensitive amplifiers located in LAr, 35 cm above the array. The signal trace, with a length of 160  $\mu$ s, is sampled at 25 MHz, while a 10  $\mu$ s window around the rising edge is sampled at 100 MHz. Digitized data are stored on a disk for the subsequent analysis.

### 5.2. Data Analysis Flow and Active Background Suppression

Since Phase I, GERDA adopted a blind-analysis procedure consisting of removing all the events within  $\pm 25$  keV of  $Q_{\beta\beta}$  from the analysis flow until all the procedures and the cuts are finalized.

The stability of detectors, as well as leakage currents and noise, are monitored through the injection of 0.05 Hz test pulses (TPs). Quality cuts based on the flatness of the baseline, polarity and time structure of the pulse, allow rejecting non-physical events, as discharge and noise bursts, while keeping 99.9% of  $Q_{\beta\beta}$  events.

The event energy reconstruction is performed with a zero-area cusp filter [75]. The energy scale is determined through weekly calibration runs with  $^{228}\text{Th}$  sources. The energy resolution at  $Q_{\beta\beta}$  in terms of FWHM is  $(4.9 \pm 1.4)$ ,  $(2.6 \pm 0.2)$ ,  $(2.9 \pm 0.1)$  keV for semi-coaxial, BEGe and IC detectors, respectively [64]. The energy resolution is stable within 0.1 keV in the whole data-taking period.

The background suppression is based on different levels. Candidate events within 10  $\mu$ s from a muon veto signal are rejected. The related dead time is  $<0.01\%$ . In the same way, events coinciding with an energy deposition in LAr are also vetoed. If at least one photoelectron within 6  $\mu$ s from a germanium detector trigger is detected by any of the photosensors of the LAr veto system, the event is classified as background. The dead time in this case is of the order of 1.8% [64]. Since the range in germanium of the two electrons of a  $\beta\beta$  decay event is of the order of 1 mm, the energy deposition is expected to be highly localized, thus featuring a single-site event (SSE). Conversely,  $\gamma$  rays (at this energy, mainly interacting via Compton scattering) are expected to deposit their energy at multiple sites featuring the so-called multi-site events (MSEs). Anti-coincidence among different Ge detectors is, therefore, exploited to discard background events. Consecutive events occurring within 1 ms are also tagged to veto time-correlated decay from primordial radioisotopes. Finally, the discrimination between SSEs and MSEs, as well as from  $\alpha$  and  $\beta$  surface events, is performed by exploiting the different characteristics of the pulse shape [76]. For BEGe and IC detectors, the PSD cut is based on the parameter  $A/E$ , where  $A$  is the maximum of the current amplitude and  $E$  is the energy. MSEs and n+ surface events show wider current pulses, thus featuring a lower  $A/E$  value with respect to SSEs. On the contrary, surface events on the p+ electrode feature a higher  $A/E$  [77]. A mono-parametric cut on both sides of the  $A/E$  distribution of SSEs is, therefore, effective at enhancing the signal-to-background ratio. Figure 7 shows the weighting potential describing the coupling of the charge with respect to the distance from the respective electrode [6] for semi-coaxial and BEGe detectors (Figure 7a) and for IC ones (Figure 7b). Due to their different geometries, semi-coaxial diodes show a more complicated pulse time structure requiring the application of an artificial neural network (ANN) to discriminate SSEs from MSEs and an additional cut on signal rise time to reject events on the p+ electrode [6,76]. Both ANN and  $A/E$  methods are trained using calibration data. The  $0\nu\beta\beta$  signal efficiency is estimated to be  $(68.8 \pm 4.1)\%$ ,  $(89.0 \pm 4.1)\%$ ,  $(90.0 \pm 1.8)\%$  for coaxial, BEGe and IC detectors, respectively [64].

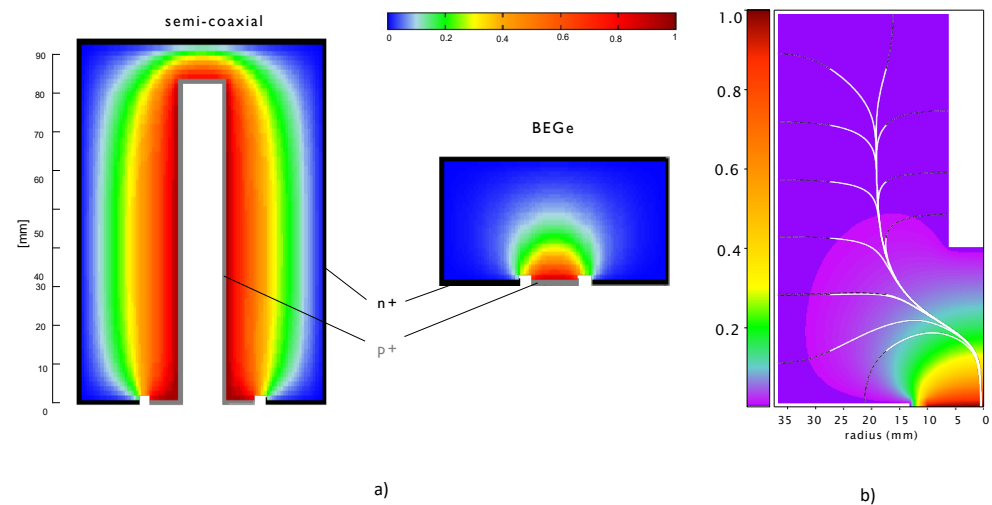


**Figure 7.** (a) Cross-sections of a GERDA coaxial (left) and BEGe (right) detector with an overlay of the corresponding weighting potentials. Figure published by Science, 2019 [6]. (b) Weighting potential for an IC detector. Figure published by EPJC, 2021 [72].

### 5.3. Statistical Analysis and $0\nu\beta\beta$ Results

The total exposure collected during GERDA Phase II is 103.7 kg·yr. The energy range around the  $Q_{\beta\beta}$  considered for the analysis goes from 1930 to 2190 keV with the exclusion of two known background peaks at  $(2104 \pm 5)$  and  $(2119 \pm 5)$  keV. After the unblinding and the application of the analysis cuts, 13 events are found in the analysis window. The energy distribution of those events is fitted assuming a flat distribution for background and a Gaussian centered at  $Q_{\beta\beta}$  with a width according to the energy resolution for a possible  $0\nu\beta\beta$  signal. Both frequentist and Bayesian analyses are applied.

The frequentist analysis is performed using a two-sided test statistics based on the profile likelihood and gives no indication for a signal. The limit on the half-life of  $^{76}\text{Ge}$  is  $T_{1/2}^{0\nu} > 1.5 \times 10^{26}$  yr (90% CL). The combined analysis of the whole Phase I and Phase II data sample, with a total exposure 127.2 kg·yr, provides the limit  $T_{1/2}^{0\nu} > 1.8 \times 10^{26}$  yr (90% CL). The limit coincides with the sensitivity, defined as the median expectation under the no signal hypothesis [64].

The background index (BI), as derived from the fit, reached the unprecedentedly low value of  $BI = 5.2_{-1.3}^{+1.6} \times 10^{-4}$  cts/(keV·kg·yr) in Phase II. The mean background expected in the signal region ( $Q_{\beta\beta} \pm 2\sigma$ ) is 0.3 counts, thus reaching the design goal of a background-free regime.

The limit obtained with the Bayesian analysis for Phase I and Phase II data is  $T_{1/2}^{0\nu} > 1.4 \times 10^{26}$  yr (90% CL). The reader is referred to [6,62–64] for the different data releases of Phase II and for further details on the statistical analysis.

In addition to standard  $0\nu\beta\beta$  searches, GERDA explored other physics topics such as the search for bosonic superweakly interacting massive particles (super-WIMPs) as keV-scale dark matter candidates [78], the search for  $0\nu\beta\beta$  decay processes accompanied with Majoron emission [79] and the study of two-neutrino double beta decay of  $^{76}\text{Ge}$  to excited states of  $^{76}\text{Se}$  [80].

## 6. The MAJORANA Experiment

The MAJORANA Collaboration searches for neutrinoless double-beta decay of  $^{76}\text{Ge}$  with High Purity Germanium detectors [81]. The MAJORANA DEMONSTRATOR [65] implements an array of 58 HPGe detectors for a total mass of 44.8 kg (14.4 kg of natural Ge detectors and 29.7 kg enriched to  $88.1 \pm 0.7\%$  in  $^{76}\text{Ge}$ ), arranged in two different modules, each contained in a low-background shield. The experiment is located at the Sanford Underground Research Facility (SURF) in Lead, South Dakota (U.S.A.), at a depth of 4300 m.w.e. Its main goal is to demonstrate a low level of background to justify the

construction of a tonne-scale experiment that would probe  $m_{\beta\beta}$  at the level of 15 meV with a nearly background-free region around the  $Q_{\beta\beta}$ . The enriched detectors are p-type, point contact (PPC) detectors [82,83] with a sub-GeV energy threshold and low capacitance; this allows low-energy physics searches as additional science channels.

Two low-background shields contain the two modules of detector arrays. These shields are made of underground electroformed copper (UGEFCu) plus an additional 5 cm of commercial C10100 copper. Outside the copper shields, an additional high-purity lead shielding, 45 cm thick, is enclosed in a region with liquid-nitrogen boil-off gas to reduce the radon contamination. An active muon veto is located outside the radon exclusion volume and is surrounded by 5 cm of borated polyethylene and 25 cm of polyethylene for neutron moderation. For each module, energy calibrations are done with  $^{228}\text{Th}$  sources inserted into the shield on a weekly basis [84]. A pictorial view of the MAJORANA experimental setup is shown in Figure 8.

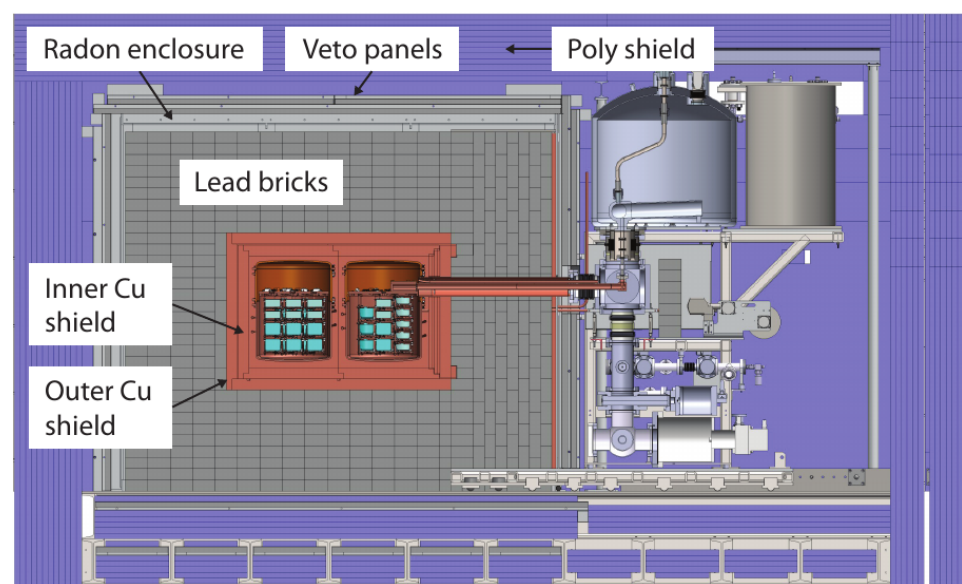


**Figure 8.** Pictorial view of the Majorana experimental setup. Figure published by J. Phys. Conf. Ser., 2020 [85].

To achieve an ultra-low background, the MAJORANA DEMONSTRATOR uses a total of 1196 kg of underground electroformed copper, not only for the innermost 5 cm of shielding surrounding the cryostat but also for the cryostats and the detector support structures. In addition, commercially available low-background materials were carefully screened and selected to be used for cabling, cryostat seals, and all electrical and thermal insulations. Low-background front-end electronics were developed as well [86].

### 6.1. Data-Taking and Event Selection

Data collected by the MAJORANA DEMONSTRATOR are divided into seven data sets (DS), from DS0 to DS6. A new data set was defined when a significant change in the experimental setup occurred, through the detector setup construction and commissioning. A letter following the data set number indicated a minor change of the experimental configuration. Data set 0 (DS0) began on 26 July 2015 with the first module of the detector array. The DS6 data acquired up to 16 April 2018 is labeled DS6a.

Data blindness was implemented through a prescaling scheme in which 31 h of open background data were followed by 93 h of blind data. The detector signals are digitized with a 14-bit 100 MHz digitizers [87], which were designed for the GRETINA experiment [88]. The signal waveforms are recorded in a 20  $\mu\text{s}$  acquisition window at the full sampling rate. Each detector had a high-gain and a low-gain signal amplification and both were digitized independently. The trigger threshold for each channel was set

independently according to the channel trigger rate, depending on the electronic noise and the initialization of the on-board trapezoidal filter (see Section 6.2). A reduction in the live time for each detector was estimated at the level of <0.1% when the initialized value of the triggering filter was negative (because of electronic noise or baseline recovery at the time of initialization due to interactions).

A physical event is represented by recorded waveforms grouped within a 4  $\mu$ s coincidence window. Events in which multiple detectors trigger are rejected. Each waveform is then processed through quality checks to remove non-physical waveforms and signals from periodic pulses. The acceptance after these quality cuts is estimated to be >99.9% for all data sets. Events within 1 s from a muon veto trigger are also rejected. Every 36 h, 30 min of data are also rejected for each module due to the filling of liquid nitrogen, which causes microphonic noise.

### 6.2. Energy Estimation

The energy estimation is done by calibrating the amplitude of the recorded signals once filtered and pole-zero adjusted. Corrections that account for ADC non-linearities and charge trapping along the drift path are applied to the acquired waveforms for each respective channel. After corrections, the energy uncertainty due to ADC effects is less than 0.1 keV. The energy resolution is also affected by drift-path-dependent charge trapping in the crystal bulk. This effect is taken into account with an additional term for the standard pole-zero adjustment:

$$\frac{1}{\tau} = \frac{1}{\tau_{PZ}} + \frac{1}{\tau_{CT}} \quad (7)$$

where  $\tau_{PZ}$  is the pole-zero time constant due to the preamplifier, and  $\tau_{CT}$  is the correction that reproduces exponential trapping of charges on the drift path. For each detector, the total pole-zero correction  $\tau$  is optimized by minimizing the full-width at half maximum (FWHM) of the 2615 keV  $^{208}\text{Tl}$  peak in calibration data: this correction improves the energy resolution of 1.4 keV on average. A fast trapezoidal filter (with a rise time of 1.0  $\mu$ s and a flat-top time of 1.5  $\mu$ s) is applied to the waveform to estimate the start time  $t_0$  and the threshold crossing time. Then the pole-zero correction and a slower trapezoidal filter (with a rise time of 4.0  $\mu$ s and a flat top time of 2.5  $\mu$ s) are applied to the original waveform. The energy of the event is estimated as the value of the waveform at a time of 0.5  $\mu$ s from the end of the flat top, relative to  $t_0$ , after having applied the above corrections and filtering.

Periodic energy calibrations are used to provide an initial linear energy scale calibration for each channel, taking into account small variations over time of the electronic noise or energy scale [84]. Then, the combination of the spectra obtained provides a more precise energy calibration through the simultaneous fit of the full energy calibration peaks at 239 keV ( $^{212}\text{Pb}$ ), 241 keV ( $^{224}\text{Ra}$ ), 277 keV ( $^{208}\text{Tl}$ ), 300 keV ( $^{212}\text{Pb}$ ), 583 keV ( $^{208}\text{Tl}$ ), 727 keV ( $^{212}\text{Bi}$ ), 861 keV ( $^{208}\text{Tl}$ ), and 2615 keV ( $^{208}\text{Tl}$ ), respectively.

Each peak is fitted with a response function  $R(E)$  given by the sum of a Gaussian function and an exponentially modified Gaussian Tail:

$$R(E) = \frac{1-f}{\sqrt{2\pi\sigma^2}} e^{-\frac{(E-\mu)^2}{2\sigma^2}} + \frac{f}{2\gamma} e^{\left(\frac{\sigma^2}{2\gamma^2} + \frac{E-\mu}{\gamma}\right)} \text{erfc}\left(\frac{\sigma}{\sqrt{2}\gamma} + \frac{E-\mu}{\sqrt{2}\sigma}\right) \quad (8)$$

where  $\sigma$  represents the smearing due to electronic noise and partial charge collection,  $\gamma$  is the decay constant of the low-energy tail, and  $f$  is the fraction of the peak shape contained in the low-energy tail. The background in the surrounding region of the peak is modeled by the sum of an error function and a continuum component given by a quadratic polynomial. The combined calibration spectrum from DS0 to DS6 is shown in the top panel of Figure 9. After having determined the FWHM at each energy peak, the FWHM is fitted with the following function of the energy  $E$ :

$$FWHM(E) = \sqrt{\Gamma_n^2 + \Gamma_F^2 E + \Gamma_q^2 E^2} \quad (9)$$

where  $\Gamma_n$ ,  $\Gamma_F$  and  $\Gamma_q$  are the terms due to the electronic noise, the Fano factor [89], and the partial charge collection, respectively. The central panel of Figure 9 shows the exposure-weighted resolution for each gamma peak and a fit to the exposure-weighted values. The exposure-weighted average resolution (FWHM) at  $Q_{\beta\beta}$  is  $(2.53 \pm 0.08)$  keV.

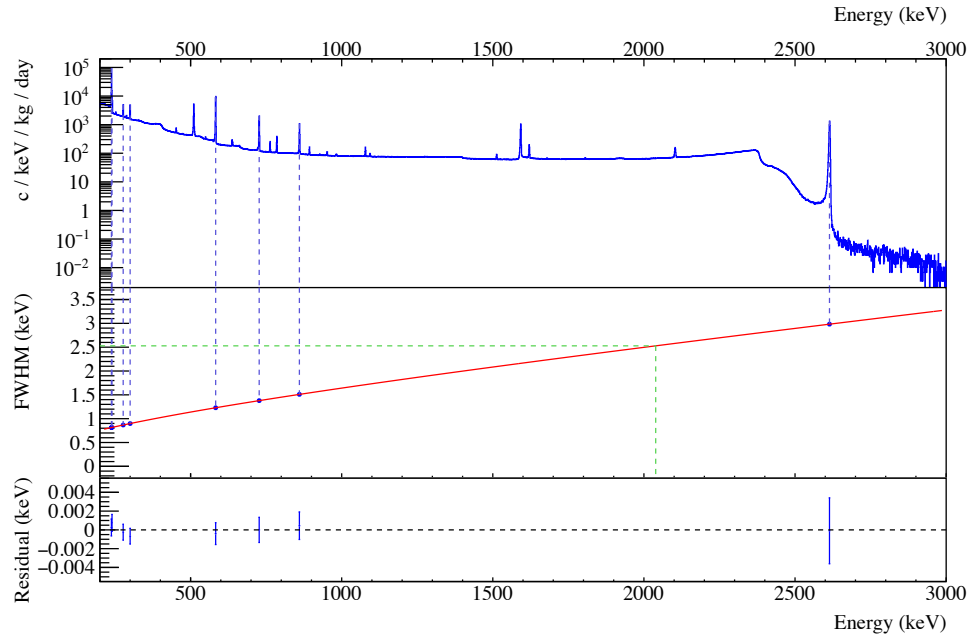


**Figure 9.** **Top:** Calibration spectrum from combined data of DS0 to DS6. **Center:** exposure-weighted resolution for all the calibration peaks and the FWHM fit function (red line). The green line indicates the exposure-weighted resolution value at 2039 keV. **Bottom:** residuals of the estimated FWHM values from the fit. Figure published by Phys. Rev. C, 2019 [7].

### 6.3. Background Suppression

The weighting potential of PPC Ge detectors is relatively smaller in the bulk of the crystal and mostly located in the vicinity of the point contact (see Figure 10, on the left). As also explained in Section 5.2, electrons interacting inside the bulk of the detectors are identified as single-site events (SSEs), as their range is limited to less than 1 mm at the energies of interest. Gamma rays, instead, interact inside the detectors mostly as multiple-site events (MSEs). This translates to a difference in the pulse shape, which allows the discrimination of the gamma-ray background. In particular, at about the same energy ( $E$ ), multi-site events have a maximum current amplitude ( $A$ ) quite smaller than single-site events; calibration data are therefore used to fit the mean value of  $A$  as a function of  $E$  for each data set and detector. The parameter  $A_{vsE}$  is defined as:

$$A_{vsE} = \frac{1}{j} (p_0 + p_1 E + p_2 E^2 - \lambda A) \tag{10}$$

where  $p_0$ ,  $p_1$  and  $p_2$  are the coefficients obtained from the fit of  $A$  as a function of  $E$  and  $\lambda$  is the calibration constant used to convert the ADC channels to energy expressed in keV.

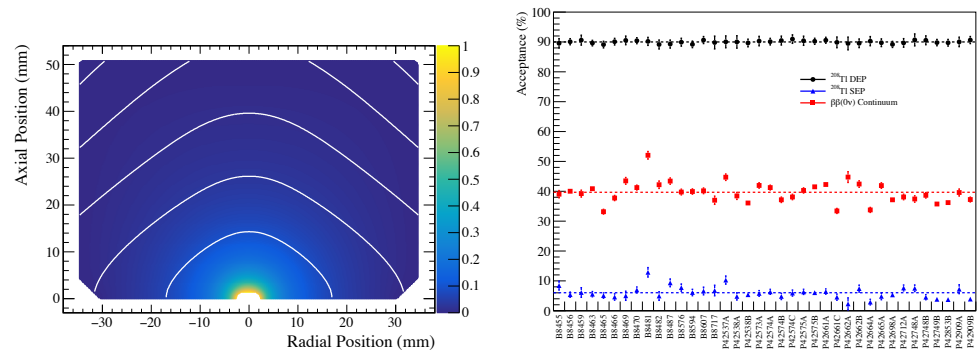


**Figure 10.** Left: weighting potential of the PPC detectors. White lines indicate equal drift times. Right: acceptance for each detector in calibration data for DS6a. Horizontal lines represent the mean values for all calibrated detectors. Figure published by Phys. Rev. C, 2019 [7].

The value of  $A_{vsE}$  is then used to establish a cut above  $\sim 1$  that would have a 90% efficiency in accepting single-site events from the 1593 keV double-escape peak (DEP) from the  $^{208}\text{Tl}$  gamma ray line at 2615 keV. The survival percentage for events in the DEP, the single-escape peak (SEP) and the Compton continuum in a 100 keV region around the  $Q_{\beta\beta}$  are shown on the right part of Figure 10 for events from DS6a and for each detector: 40% of Compton events are accepted while about 6% of multi-site events from the SEP are retained. The main systematic uncertainties in the  $A_{vsE}$  estimation are due to the difference between the position distribution of simulated events and the interactions from the calibration sources, the time-variation in the SSE acceptance and the energy dependence of the cut acceptance [90].

External  $\alpha$  particles with MeV energies have a range of tens of  $\mu\text{m}$  in Ge detectors. The PPC Ge detectors of MAJORANA have lithiated dead layers (1.1 mm thick) over the surface and a passivated surface on the face with the point contact. As the dead layers are much thicker than their range,  $\alpha$  particles impinging the lithiated surfaces cannot penetrate inside the active volume. On the contrary, they can penetrate the passivated surface and deposit their energy in the active region of the detectors. The holes near the passivated surface are trapped and later released in a time that is much longer than the rise time of events occurring in the bulk. This degrades the measured energy for  $\alpha$  particles, contributing to the background near the  $Q_{\beta\beta}$  value but the difference in rise time with respect to events occurring in the bulk allows for their discrimination. A cut is defined, based on the slope  $\Delta$  between the average value of the two  $1\text{ }\mu\text{s}$ -wide regions, which start either  $2\text{ }\mu\text{s}$  after the time the waveform reaches 97% of its maximum ( $t_{97}$ ) or  $1\text{ }\mu\text{s}$  before the end of the waveform ( $t_{\text{max}}$ ). The parameter DCR (Delayed Charge Recovery) is defined as the following:

$$\text{DCR} = \frac{\int_{t_{\text{max}}-1\mu\text{s}}^{t_{\text{max}}} V(t)dt - \int_{t_{97}+2\mu\text{s}}^{t_{97}+3\mu\text{s}} V(t)dt}{t_{\text{max}} - t_{97}} - \Delta \quad (11)$$

and ensures 99.9% acceptance of the Compton events from calibration data near the  $Q_{\beta\beta}$  value. The acceptance of the cut is estimated for each data set.

#### 6.4. $0\nu\beta\beta$ Search Results

The characteristics and the efficiencies values are evaluated for each data set. In addition to the efficiencies for background rejection  $\epsilon_{A_{vsE}}$  and  $\epsilon_{DCR}$ , the efficiency  $\epsilon_{\text{cont}}$  of detecting the full energy of  $0\nu\beta\beta$  events is combined together with the previous ones. The total efficiency weighted with the exposure of all data sets is  $0.810^{+0.031}_{-0.032}$ . The  $0\nu\beta\beta$  ROI is optimized for each data set using the peak shape parameters and background index.  $\epsilon_{\text{res}}$  represents the fraction of  $0\nu\beta\beta$  events falling inside the optimal ROI for each data set. The exposure weighted value for  $\epsilon_{\text{res}}$  over all data sets is  $0.900 \pm 0.007$ .

A total of 26 kg·yr exposure was collected from DS0 to DS6 of which 11.85 kg·yr were blinded across the energy spectrum. The energy spectrum above 100 keV relative to the full

enriched detector exposure is shown in Figure 11 (left), with only data cleaning and muon veto cuts (in black) and with all cuts applied (in red). The inset shows the background events between 1950 and 2350 keV, where a flat component is expected (from background simulations with the MAGE software [91] based on GEANT4 [92]) with the exclusion of  $\pm 5$  KeV of the 2103 keV (single-escape peak from  $^{208}\text{Tl}$ ), 2118 keV and 2204 keV (gammas from  $^{214}\text{Bi}$ ) peaks. The predicted background in this region is  $(6.1 \pm 0.8) \times 10^{-3}$  counts/(keV·kg·yr) in the exposure weighted optimal ROI of 4.13 keV and is consistent with  $^{208}\text{Tl}$  contamination in components larger than assay values, whose origin is under investigation.

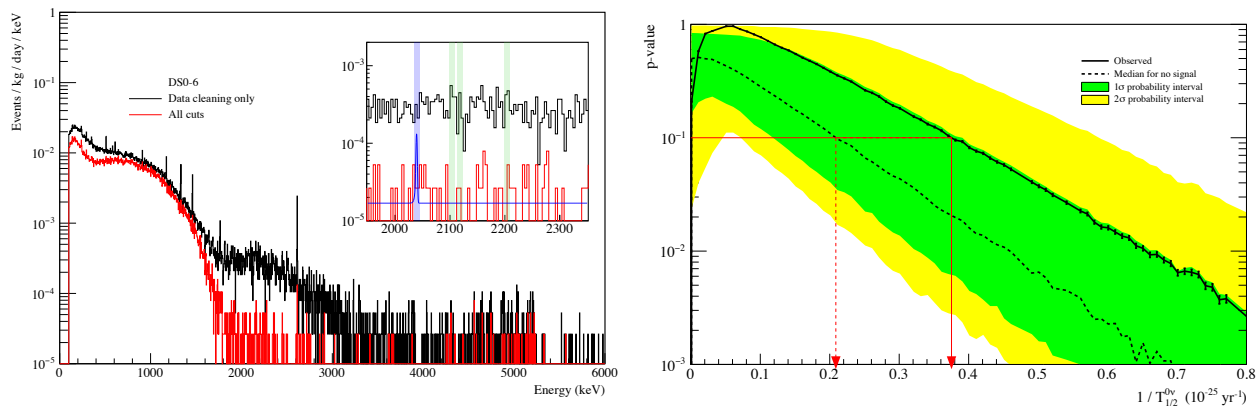


**Figure 11.** Left: energy spectrum above 100 keV with only data cleaning and muon veto cuts (black) and after all cuts (red). The blue curve shows the fitted background from the unshaded regions in the inset and the 90% C.L. upper limit on the counts from a  $0\nu\beta\beta$  signal. Right: the  $p$ -value as a function of the  $0\nu\beta\beta$  half-life estimated from the unbinned frequentist profile-likelihood method (solid black). The median sensitivity is shown as a dashed black line, and the shaded bands represent the 1 and  $2\sigma$  intervals. Figure published by Phys. Rev. C, 2019 [7].

The limit on the half-life of the  $0\nu\beta\beta$  decay of  $^{76}\text{Ge}$  (considered as a Poisson process) is estimated with a Feldman–Cousins approach (see Reference [93]) with 0.65 expected background events and 1 event observed in the ROI at 2040 keV. The value of the 90% C.L. lower limit is  $2.5 \times 10^{25}$  yr. Based on an unbinned, extended profile likelihood method based on RooStats (see References [62,94,95]), the median sensitivity at 90% C.L. is  $4.8 \times 10^{25}$  yr, as shown in Figure 11. The  $p$ -value distribution of the half-life is  $T_{1/2}^{0\nu} > 2.7 \times 10^{25}$  yr at 90% C.L. In this analysis, the half-life is a common parameter for all data sets, while the peak shape parameters and signal efficiencies are constrained as a Gaussian nuisance term for each data set. The corresponding upper limit on the number of signal events at 90% C.L. is 3.8. A Bayesian statistical analysis was also performed using Markov chain Monte Carlo simulations in RooStats with the same likelihood function. With a flat prior on  $1/T_{0\nu}^{1/2}$ , the Bayesian limit on the half-life is  $2.5 \times 10^{25}$  yr for a 90% credible interval.

Based on a range of nuclear matrix elements for  $^{76}\text{Ge}$  [22,96–99], phase-space factors of  $2.36 \times 10^{-15}/\text{yr}$  ([32]) or  $2.37 \times 10^{-15}/\text{yr}$  ([100]), and a value of  $g_A = 1.27$ , the limit on the half-life is converted in a range of upper limits for the effective neutrino mass given by  $m_{\beta\beta} < (200\text{--}433)$  meV [7].

## 7. The LEGEND Project

Building upon the success of the GERDA and MAJORANA experiments, the LEGEND (Large Enriched Germanium Detector for Neutrinoless  $\beta\beta$  Decay) Collaboration [66] aims at building a  $^{76}\text{Ge}$ -based neutrinoless double beta decay experiment with a sensitivity of the half-life beyond  $10^{28}$  years, to fully span the inverted neutrino mass ordering region.

MAJORANA and GERDA have already proven to have the best energy resolution (see Section 6.2), the lowest background index and the best sensitivity in the field (see Section 5.3). The LEGEND experiment will benefit from the knowledge and from the technological achievements of the two Collaborations, as well as from the contributions of new joining groups.

LEGEND will inherit the shielding concept implemented in GERDA with the use of a water Cherenkov veto and the depletion of bare germanium detectors in an instrumented LAr volume simultaneously acting as a coolant medium and active veto. The low-noise readout electronic developed by the MAJORANA Collaboration has proven to be successful in improving the PSD performances as well as in lowering the threshold thus resulting in an unprecedented low energy resolution. Moreover, the careful selection and radiopurity control of the employed materials allowed MAJORANA to reach a similar background level with respect to GERDA.

The natural steps toward reaching higher sensitivities consist of increasing the detector mass while further reducing the background, aiming at performing a background-free measurement at larger exposures.

The LEGEND project will proceed in two steps: in the first phase, 200 kg of enriched germanium detectors will be deployed in the existing GERDA facility at LNGS. By reducing the background index of about a factor of three with respect to the GERDA final level (i.e., from 1.5 cts/(FWHM·t·yr) to 0.5 cts/(FWHM·t·yr)) and with an exposure of 1 t·yr, LEGEND-200 will be able to reach a sensitivity of about  $10^{27}$  yr at 90% C.L. The data-taking is expected to start by the end of 2021.

In the second phase, the enriched germanium mass will be increased up to 1000 kg. By lowering the background to 0.025 cts/(FWHM·t·yr) and with an exposure of 10 t·yr, LEGEND-1000 will be able to reach a  $3\sigma$  half-life discovery sensitivity of  $1.3 \times 10^{28}$  yr (see Figure 12). The location of the LEGEND-1000 phase will be selected in order to keep the cosmogenic activation background as low as possible and within the required background level.

In the next sections, we will present the project and we will discuss the main issues addressed by the LEGEND Collaboration.

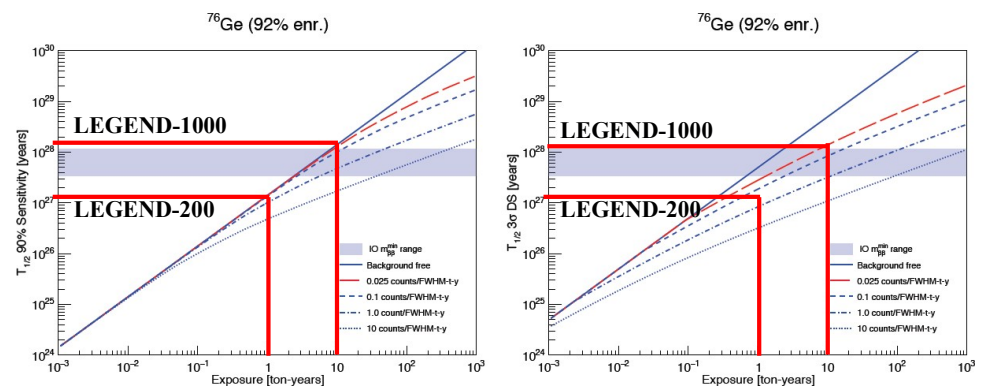


**Figure 12.** Sensitivity as a function of exposure and background for an isotopic enrichment fraction in  $^{76}\text{Ge}$  of 92% and for (left) a 90% C.L. limit setting and (right) a  $3\sigma$  signal discovery. Plots from [101].

### 7.1. LEGEND-200 Germanium Detectors and Experimental Setup

The existing GERDA cryostat is large enough to accommodate up to 200 kg of detectors divided into 19 strings for a total diameter of 500–550 mm (see Figure 13a) [66]. The approach of reusing the GERDA experimental apparatus will assure a timely start of data-taking with a world-leading sensitive experiment.

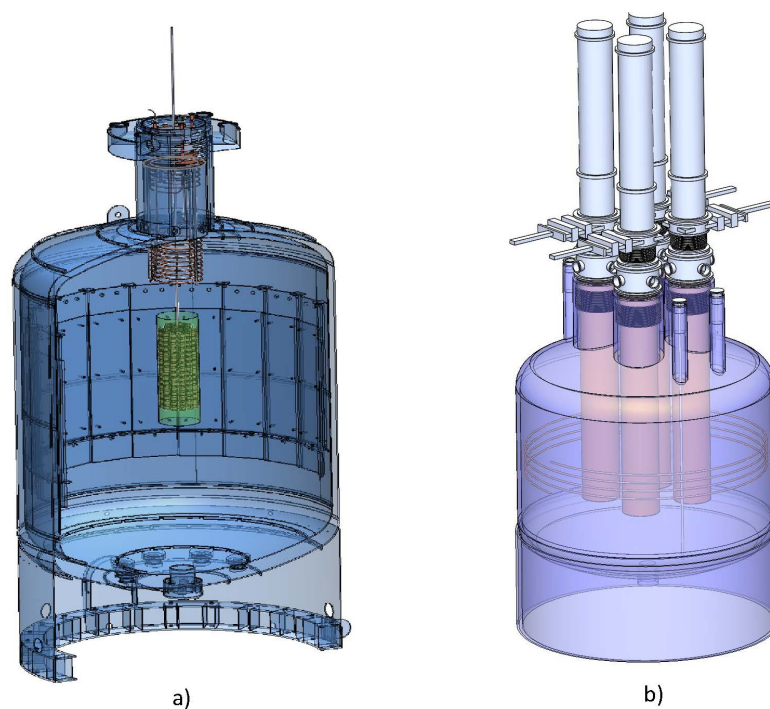


**Figure 13.** Experimental setup of the LEGEND-200 (a) and LEGEND-1000 (b) phase, respectively.

LEGEND-200 will deploy 20 kg of BEGe and 9.4 kg of ICPC detectors (see Figure 5b,c) from GERDA and 28 kg of PPC detectors from MAJORANA. In addition, nearly 140 kg of newly produced ICPC detectors will be added. As discussed in Sections 5.1 and 5.2, ICPCs feature a new geometry with respect to the previously used germanium detectors. As shown in Figure 5c, a small  $p^+$  electrode is placed on the opposite face with respect to the bore hole and the  $n^+$  outer contact covers all the remaining surfaces (cylindrical part and bore hole). Like semi-coaxial detectors, ICPCs can be manufactured with a larger mass ( $\sim 2$  kg) with respect to BEGes ( $\sim 0.8$  kg) and PPCs ( $\sim 0.85$  kg). This allows increasing the active mass while reducing the amount of nearby materials contributing to the background, such as cables, electronics and holders. Moreover, the reduced surface-to-volume ratio with respect to smaller detectors, makes ICPCs less susceptible to surface effects. Furthermore, because of the long drift time inside the crystal and the small  $p^+$  electrode, the energy resolution and the pulse shape characteristics are very similar to BEGe and PPC [102], making this new type of HPGe suitable for  $0\nu\beta\beta$  decay experiments.

As explained in Section 5.2, during the 2018 upgrade, five  $^{76}\text{Ge}$  enriched ICPC detectors were deployed in the GERDA cryostat and operated in LAr for the first time until the end of the data-taking in 2019. After being tested and characterized, they showed energy resolution and background rejection capability comparable with BEGes while having a larger mass by a factor of three [64,72].

### 7.2. Readout Electronics

LEGEND-200 will use a resistive-feedback charge-sensitive amplifier (CSA) operated at cryogenic temperature in LAr. CSA is divided into two stages in order to meet the background requirements. The first stage is the low mass front end (LMFE [103]), a custom-made low-background circuit based on the front-end used in MAJORANA where a junction gate field-effect transistor (JFET) is installed. LMFE is made of ultra-clean materials ( $<1 \mu\text{Bq}/\text{kg}$ ) due to its close vicinity to the detectors. The second stage is a differential amplifier  $\sim 30\text{--}150$  cm away from the first stage; in this case, a slightly higher activity ( $50 \mu\text{Bq}$ ) can be tolerated. The amplifier is based on the one already used in GERDA [104] and the two stages are connected using four custom-made low-mass coaxial-cables. The CSA is designed to have electronic noise  $<1$  keV FWHM, an energy resolution of  $\leq 2.5$  keV

at  $Q_{\beta\beta}$ , a fast rise time of  $\leq 100$  ns to allow powerful pulse shape discrimination analysis and high linearity up to 10 MeV for alpha particles rejection [105].

For LEGEND-1000, in order to have the same performance with lower background contribution, an ASIC preamplifier to be placed near the detectors is being studied.

### 7.3. Background Mitigation Techniques

The electroformed copper (UGEFCu) employed in the MAJORANA experiment (see Section 6), shows a uranium and thorium decay chain activity of  $<0.1 \mu\text{Bq}/\text{kg}$  [106]. This value is at least one order of magnitude lower than that of the most commercial oxygen-free, high-conductivity (OFHC) copper used in the external layers of the MAJORANA shielding. UGEFCu is produced at Pacific Northwest National Laboratory and SURF, where it is also stored underground to minimize the possibility of cosmogenic activation producing  $^{60}\text{Co}$ , whose decay yields photons above the Ge  $Q_{\beta\beta}$  value [107]. The employment of electroformed copper is going to improve the GERDA radiopurity for LEGEND-200.

As introduced above, in both LEGEND phases, HPGe detectors will be operated in a LAr-filled cryostat. LAr acts as a coolant for germanium detectors and a passive shield against external radiation. Moreover, an active veto system in GERDA was used to discard background events (such as neutrons and photons) depositing energy in LAr and making it scintillating in coincidence with a signal in the Ge diodes. As shown in Figure 14, LEGEND-200 will use a similar design, although with a different geometry, to deal with the increased number of detectors in the array while maximizing the light collection efficiency. Further enhancement of the light yield and attenuation length can be reached by improving LAr purity and by applying Xe doping [107].

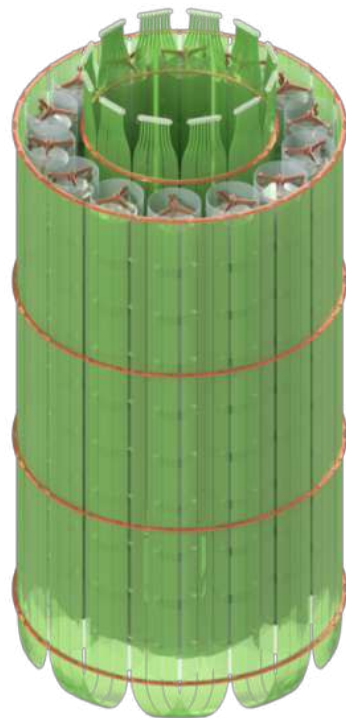


**Figure 14.** Instrumentation of the LAr volume around the detectors strings in LEGEND-200.

The use of detector holders made from polyethylene naphthalate (PEN) will further improve the background rejection capability. PEN is a thermoplastic material with scintillating properties and an emission spectrum that peaks in the blue region at 425 nm. Its scintillation yield is 2.5 times lower than standard plastic scintillators, but it has other appealing features such as its very favorable mechanical properties at cryogenic temperature (77 K) and its radiopurity. Moreover, PEN shifts the LAr 128 nm photons to a higher wavelength, making it detectable with standard photodetectors [108]. By replacing the

Si-made, nontransparent detector holders previously used in GERDA with PEN supports, it would be possible to improve the light collection in the vicinity of the detectors while at the same time exploiting PEN self-vetoing capabilities [109]. The employment of Pulse Shape Discrimination techniques with PEN is also feasible [108]. In this way, it could be possible to more efficiently reduce the background due to surface events and detect LAr scintillating light close to the detectors. PEN holders specifically designed and optimized to reduce the total mass in contact with the detectors are being produced and will be employed in LEGEND-200 [109].

An important source of background in LEGEND-200 is the  $^{42}\text{Ar}$ , a cosmogenically produced Ar isotope that  $\beta$ -decays to  $^{42}\text{K}$ . The distribution of  $^{42}\text{K}$  in LAr is quite likely to be inhomogeneous due to its drift in the electric field generated by high-voltage cables and detectors and also convective motion. Because of its very high  $\beta^-$   $Q$ -value of 3.5 MeV, higher than  $Q_{\beta\beta}$ ,  $^{42}\text{K}$  contributes to the backgrounds in  $0\nu\beta\beta$  searches. In LEGEND-200, the drift of  $^{42}\text{K}$  towards germanium detectors will be reduced by nylon shrouds around each detector's columns (following the GERDA approach). LEGEND-1000, because of more stringent background requirements, will make use of underground Ar, which is free in  $^{42}\text{Ar}$ , thus almost completely removing the  $^{42}\text{K}$  background.

In addition to the aforementioned techniques, LEGEND will follow the GERDA and MAJORANA approach in the background reduction techniques through the selection of SSEs,  $0\nu\beta\beta$ -like events. The rejection of MSEs will be performed by applying anti-coincidence cuts and PSD methods, as illustrated in Sections 5.2 and 6.3. Figure 15a shows the expected effectiveness of these cuts in terms of the reduction of the  $\gamma$  rate due to the  $^{238}\text{U}$ ,  $^{232}\text{Th}$  and  $^{40}\text{K}$  chains [110]. Figure 15b shows the projected contribution of the different sources to the overall total background. A total background of  $1 \times 10^{-4}$  cts/(keV·kg·yr) is anticipated [111].

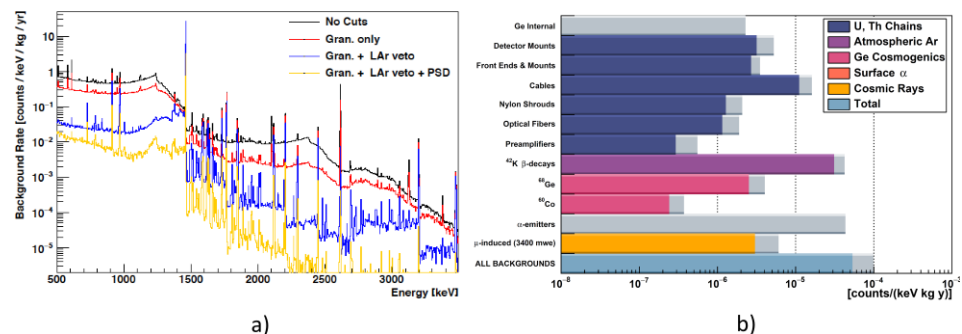


**Figure 15.** (a) Reduction of the  $\gamma$  rate due to the  $^{238}\text{U}$ ,  $^{232}\text{Th}$  and  $^{40}\text{K}$  chains. Figure published by J. Phys. Conf. Ser., 2020 [110]. (b) Projected contribution of the different sources to the overall total background. Grey bars indicate  $1\sigma$  uncertainties of the background contributions due to screening measurements and Monte Carlo simulations. A total background of  $1 \times 10^{-4}$  cts/(keV·kg·yr) is anticipated. Figure published by J. Phys. Conf. Ser., 2020 [111].

## 8. Conclusions

In this paper, we reviewed the successful story of the experiments employing germanium semiconductor detectors in the search for the  $0\nu\beta\beta$  transition of  $^{76}\text{Ge}$ . Starting from the pioneering work conducted by E. Fiorini and collaborators in 1967, we followed the technology evolution from the original Ge(Li) diodes to the development of the modern HPGe detectors featuring a negligible intrinsic background contamination and impressive background rejection capabilities and energy resolution. Parallel to the development of the detectors, an outstanding lowering of the background index by about eight orders of magnitude led to an increase in the sensitivity of the experiment by about six orders of magnitude in 50 years. Currently, the GERDA experiment, implementing the use of bare Ge diodes immersed in LAr, succeeded at reaching the background-free regime, thus achieving the best sensitivity in the field with a lower exposure with respect to competitors.

The joint venture between GERDA and MAJORANA Collaborations led to establishing the LEGEND project, aiming at building a ton-scale experiment to fully span the inverted mass ordering region with a world-leading and timely competitive program.

**Author Contributions:** Writing—original draft, V.D., N.D.M., C.M., M.M., F.S.; Writing—review and editing, V.D., N.D.M., M.B.J., M.L., C.M., M.M., F.S., C.V. All authors have read and agreed to the published version of the manuscript.

**Funding:** This research received no external funding.

**Institutional Review Board Statement:** Not applicable.

**Informed Consent Statement:** Not applicable.

**Data Availability Statement:** Data sharing not applicable.

**Acknowledgments:** The authors would like to thank Riccardo Brugnera and Steven Ray Elliott for their suggestions and comments.

**Conflicts of Interest:** The authors declare no conflict of interest.

## References

1. Fukuda, Y.; Hayakawa, T.; Ichihara, E.; Inoue, K.; Ishihara, K.; Ishino, H.; Itow, Y.; Kajita, T.; Kameda, J.; Kasuga, S.; et al. Evidence for Oscillation of Atmospheric Neutrinos. *Phys. Rev. Lett.* **1998**, *81*, 1562–1567. [[CrossRef](#)]
2. Eguchi, K.; Enomoto, S.; Furuno, K.; Goldman, J.; Hanada, H.; Ikeda, H.; Ikeda, K.; Inoue, K.; Ishihara, K.; Itoh, W.; et al. First Results from KamLAND: Evidence for Reactor Antineutrino Disappearance. *Phys. Rev. Lett.* **2003**, *90*, 021802. [[CrossRef](#)] [[PubMed](#)]
3. McDonald, A.B. Nobel Lecture: The Sudbury Neutrino Observatory: Observation of flavor change for solar neutrinos. *Rev. Mod. Phys.* **2016**, *88*, 030502. [[CrossRef](#)]
4. Kajita, T. Nobel Lecture: Discovery of atmospheric neutrino oscillations. *Rev. Mod. Phys.* **2016**, *88*, 030501. [[CrossRef](#)]
5. Cowan, C.L.; Reines, F.; Harrison, F.B.; Kruse, H.W.; McGuire, A.D. Detection of the Free Neutrino: A Confirmation. *Science* **1956**, *124*, 103–104. [[CrossRef](#)]
6. Agostini, M.; Bakalyarov, A.M.; Balata, M.; Barabanov, I.; Baudis, L.; Bauer, C.; Bellotti, E.; Belogurov, S.; Bettini, A.; Bezrukov, L.; et al. Probing Majorana neutrinos with double- $\beta$  decay. *Science* **2019**, *365*, 1445–1448. [[CrossRef](#)]
7. Alvis, S.I.; Arnquist, I.J.; Avignone, F.T.; Barabash, A.S.; Barton, C.J.; Basu, V.; Bertrand, F.E.; Bos, B.; Busch, M.; Buuck, M.; et al. Search for neutrinoless double- $\beta$  decay in  $^{76}\text{Ge}$  with 26 kg yr of exposure from the Majorana Demonstrator. *Phys. Rev. C* **2019**, *100*, 025501. [[CrossRef](#)]
8. Azzolini, O.; Beeman, J.W.; Bellini, F.; Beretta, M.; Biassoni, M.; Brofferio, C.; Bucci, C.; Capelli, S.; Cardani, L.; Carniti, P.; et al. Final result of CUPID-0 phase-I in the search for the  $^{82}\text{Se}$  Neutrinoless Double- $\beta$  Decay. *Phys. Rev. Lett.* **2019**, *123*, 032501. [[CrossRef](#)]
9. Alenkov, V.; Bae, H.W.; Beyer, J.; Boiko, R.S.; Boonin, K.; Buzanov, O.; Chanthima, N.; Cheoun, M.K.; Chernyak, D.M.; Choe, J.S.; et al. First Results from the AMoRE-Pilot neutrinoless double beta decay experiment. *Eur. Phys. J. C* **2019**, *79*, 791. [[CrossRef](#)]
10. Arnold, R.; Augier, C.; Baker, J.D.; Barabash, A.S.; Basharina-Freshville, A.; Blondel, S.; Blot, S.; Bongrand, M.; Brudanin, V.; Busto, J.; et al. Results of the search for neutrinoless double- $\beta$  decay in  $^{100}\text{Mo}$  with the NEMO-3 experiment. *Phys. Rev. D* **2015**, *92*, 072011. [[CrossRef](#)]
11. Armengaud, E.; Augier, C.; Barabash, A.S.; Bellini, F.; Benato, G.; Benoît, A.; Beretta, M.; Bergé, L.; Billard, J.; Borovlev, Y.A.; et al. The CUPID-Mo experiment for neutrinoless double-beta decay: Performance and prospects. *Eur. Phys. J. C* **2020**, *80*, 44. [[CrossRef](#)]
12. Adams, D.Q.; Alduino, C.; Alfonso, K.; Avignone, F.T., III; Azzolini, O.; Bari, G.; Bellini, F.; Benato, G.; Biassoni, M.; Branca, A.; et al. Improved Limit on Neutrinoless Double-Beta Decay in  $^{130}\text{Te}$  with CUORE. *Phys. Rev. Lett.* **2020**, *124*, 122501. [[CrossRef](#)] [[PubMed](#)]
13. Andringa, S.; Arushanova, E.; Asahi, S.; Askins, M.; Auty, D.J.; Back, A.R.; Barnard, Z.; Barros, N.; Beier, E.W.; Bialek, A.; et al. Current Status and Future Prospects of the SNO+ Experiment. *Adv. High Energy Phys.* **2016**, *2016*, 6194250. [[CrossRef](#)]
14. Anton, G.; Badhrees, I.; Barbeau, P.S.; Beck, D.; Belov, V.; Bhatta, T.; Breidenbach, M.; Brunner, T.; Cao, G.F.; Cen, W.R.; et al. Search for Neutrinoless Double- $\beta$  Decay with the Complete EXO-200 Dataset. *Phys. Rev. Lett.* **2019**, *123*, 161802. [[CrossRef](#)] [[PubMed](#)]
15. Gando, A.; Gando, Y.; Hachiya, T.; Hayashi, A.; Hayashida, S.; Ikeda, H.; Inoue, K.; Ishidoshiro, K.; Karino, Y.; Koga, M.; et al. Search for Majorana Neutrinos near the Inverted Mass Hierarchy Region with KamLAND-Zen. *Phys. Rev. Lett.* **2016**, *117*, 082503. [[CrossRef](#)] [[PubMed](#)]
16. Martín-Albo, J.; Muñoz Vidal, J.; Ferrario, P.; Nebot-Guinot, M.; Gómez-Cadenas, J.J.; Álvarez, V.; Azevedo, C.D.R.; Borges, F.I.G.; Cárceles, S.; Cebrián, S.; et al. Sensitivity of NEXT-100 to Neutrinoless Double Beta Decay. *JHEP* **2016**, *5*, 159. [[CrossRef](#)]
17. Fiorini, E.; Pullia, A.; Bertolini, G.; Cappellani, F.; Restelli, G. A search for lepton non-conservation in double beta decay with a germanium detector. *Phys. Lett. B* **1967**, *25*, 602–603. [[CrossRef](#)]

18. Goeppert-Mayer, M. Double beta-disintegration. *Phys. Rev.* **1935**, *48*, 512–516. [[CrossRef](#)]
19. Furry, W.H. On transition probabilities in double beta-disintegration. *Phys. Rev.* **1939**, *56*, 1184–1193. [[CrossRef](#)]
20. Barabash, A. Precise Half-Life Values for Two-Neutrino Double- $\beta$  Decay: 2020 review. *Universe* **2020**, *6*, 159. [[CrossRef](#)]
21. Doi, M.; Kotani, T.; Nishiura, H.; Okuda, K.; Takasugi, E. Neutrino Mass, the Right-Handed Interaction and the Double Beta Decay. II: General Properties and Data Analysis. *Prog. Theor. Phys.* **1981**, *66*, 1765–1788. [[CrossRef](#)]
22. Menéndez, J.; Poves, A.; Caurier, E.; Nowacki, F. Disassembling the nuclear matrix elements of the neutrinoless  $\beta\beta$  decay. *Nucl. Phys. A* **2009**, *818*, 139–151. [[CrossRef](#)]
23. Šimkovic, F.; Rodin, V.; Faessler, A.; Vogel, P.  $0\nu\beta\beta$  and  $2\nu\beta\beta$  nuclear matrix elements, quasiparticle random-phase approximation, and isospin symmetry restoration. *Phys. Rev. C* **2013**, *87*, 045501. [[CrossRef](#)]
24. Barea, J.; Kotila, J.; Iachello, F.  $0\nu\beta\beta$  and  $2\nu\beta\beta$  nuclear matrix elements in the interacting boson model with isospin restoration. *Phys. Rev. C* **2015**, *91*, 034304. [[CrossRef](#)]
25. Dolinski, M.J.; Poon, A.W.P.; Rodejohann, W. Neutrinoless Double-Beta Decay: Status and Prospects. *Ann. Rev. Nucl. Part Sci.* **2019**, *69*, 219–251. [[CrossRef](#)]
26. Šimkovic, F.; Pantis, G.; Vergados, J.D.; Faessler, A. Additional nucleon current contributions to neutrinoless double  $\beta$  decay. *Phys. Rev. C* **1999**, *60*, 055502. [[CrossRef](#)]
27. Deppisch, F.F.; Hati, C.; Patra, S.; Pritimita, P.; Sarkar, U. Neutrinoless double beta decay in left-right symmetric models with a universal seesaw mechanism. *Phys. Rev. D* **2018**, *97*, 035005. [[CrossRef](#)]
28. Armstrong, W.R.; Chang, C.; Hafidi, K.; Lisovenko, M.; Novosad, V.; Pearson, J.; Polakovic, T.; Wang, G.; Yefremenko, V.; Zhang, J.; et al. CUPID Pre-CDR. Working Paper. 2019. Available online: <https://hal.archives-ouvertes.fr/hal-02283520> (accessed on 1 August 2021).
29. Albert, J.B.; Anton, G.; Badhrees, I.; Barbeau, P.S.; Bayerlein, R.; Beck, D.; Belov, V.; Breidenbach, M.; Brunner, T.; Cao, G.F.; et al. Search for Neutrinoless Double-Beta Decay with the Upgraded EXO-200 Detector. *Phys. Rev. Lett.* **2018**, *120*, 072701. [[CrossRef](#)]
30. Monrabal, F.; Gómez-Cadenas, J.J.; Toledo, J.F.; Álvarez, V.; Benlloch-Rodríguez, J.M.; Cárcel, S.; Carrión, J.V.; Esteve, R.; Felkai, R.; Herreroet, V.; et al. The NEXT White (NEW) detector. *JINST* **2018**, *13*, P12010. [[CrossRef](#)]
31. Gando, Y. First results of KamLAND-Zen 800. *J. Phys. Conf. Ser.* **2020**, *1468*, 012142. [[CrossRef](#)]
32. Kotila, J.; Iachello, F. Phase space factors for double- $\beta$  decay. *Phys. Rev. C* **2012**, *85*, 034316. [[CrossRef](#)]
33. Stoica, S.; Mirea, M. New calculations for phase space factors involved in double- $\beta$  decay. *Phys. Rev. C* **2013**, *88*, 037303. [[CrossRef](#)]
34. Primakoff, H.; Rosen, S. Alpha, Beta, and Gamma-Ray Spectroscopy. *Phys. Today* **1965**, *18*, 76. [[CrossRef](#)]
35. Fiorini, E.; Pullia, A.; Bertolini, G.; Cappellani, F.; Restelli, G. An underground experiment on neutrinoless double beta-decay. *Lett. Nuovo Cimento (1969–1970)* **1970**, *3*, 149–152. [[CrossRef](#)]
36. Fiorini, E.; Pullia, A.; Bertolini, G.; Cappellani, F.; Restelli, G. Neutrinoless double-beta decay of  $^{76}\text{Ge}$ . *Il Nuovo Cimento A (1965–1970)* **1973**, *13*, 747–763. [[CrossRef](#)]
37. Avignone, F.T.; Elliott, S.R. The Search for Double Beta Decay With Germanium Detectors: Past, Present, and Future. *Front. Phys.* **2019**, *7*, 6. [[CrossRef](#)]
38. Bellotti, E.; Cremonesi, O.; Fiorini, E.; Liguori, C.; Pullia, A.; Sverzellati, P.P.; Zanotti, L. New limits on double beta decay of  $^{76}\text{Ge}$ . *Phys. Lett. B* **1984**, *146*, 450–456. [[CrossRef](#)]
39. Bellotti, E.; Cremonesi, O.; Fiorini, E.; Liguori, C.; Pullia, A.; Sverzellati, P.P.; Zanotti, L. The milano experiment on lepton number nonconservation in double beta-decay of  $^{76}\text{Ge}$ . *Il Nuovo Cimento A (1965–1970)* **1986**, *95*, 1–46. [[CrossRef](#)]
40. Forster, A.; Kwon, H.; Markey, J.K.; Boehm, F.; Henrikson, H.E. Low background study of the neutrinoless double beta decay of  $^{76}\text{Ge}$  and upper limit for neutrino mass. *Phys. Lett. B* **1984**, *138*, 301–303. [[CrossRef](#)]
41. Simpson, J.J.; Jagam, P.; Campbell, J.L.; Malm, H.L.; Robertson, B.C. New Limit for Neutrinoless Double  $\beta$  Decay of  $^{76}\text{Ge}$ . *Phys. Rev. Lett.* **1984**, *53*, 141–143. [[CrossRef](#)]
42. Fisher, P.; Boehm, F.; Bovet, E.; Egger, J.P.; Henrikson, H.; Gabathuler, K.; Mitchell, L.W.; Reusser, D.; Treichel, M.; Vuilleumier, J.L. A search for double beta decay in  $^{76}\text{Ge}$ . *Phys. Lett. B* **1989**, *218*, 257–262. [[CrossRef](#)]
43. Reusser, D.; Treichel, M.; Boehm, F.; Fisher, P.; Gabathuler, K.; Henrikson, H.E.; Jörgens, V.; Mitchell, L.W.; Nussbaum, C.; Vuilleumier, J.L. Final report on the search for neutrinoless double- $\beta$  decay of  $^{76}\text{Ge}$  from the Gotthard underground experiment. *Phys. Rev. D* **1992**, *45*, 2548–2551. [[CrossRef](#)]
44. Avignone, F.T.; Brodzinski, R.L.; Brown, D.P.; Evans, J.C.; Hensley, W.K.; Reeves, J.H.; Wogman, N.A. New Limits on the Neutrino Mass, Lepton Conservation, and No-Neutrino Double Beta Decay of  $^{76}\text{Ge}$ . *Phys. Rev. Lett.* **1983**, *50*, 721–724. [[CrossRef](#)]
45. Avignone, F.T.; Brodzinski, R.L.; Brown, D.P.; Evans, J.C.; Hensley, W.K.; Miley, H.S.; Reeves, J.H.; Wogman, N.A. Ultralow-Background Study of Neutrinoless Double  $\beta$  Decay of  $^{76}\text{Ge}$ : New Limit on the Majorana Mass of  $\nu_e$ . *Phys. Rev. Lett.* **1985**, *54*, 2309–2312. [[CrossRef](#)]
46. Avignone, F.T.; Brodzinski, R.L.; Evans, J.C.; Hensley, W.K.; Miley, H.S.; Reeves, J.H. Search for the double- $\beta$  decay of  $^{76}\text{Ge}$ . *Phys. Rev. C* **1986**, *34*, 666–677. [[CrossRef](#)]
47. Caldwell, D.O.; Eisberg, R.M.; Grumm, D.M.; Witherell, M.S.; Goulding, F.S.; Smith, A.R. Limits on neutrinoless  $\beta\beta$  decay, including that with majoron emission. *Phys. Rev. Lett.* **1987**, *59*, 419–422. [[CrossRef](#)] [[PubMed](#)]
48. Caldwell, D.O. Double beta decay-present and future. *J. Phys. G Nucl. Part Phys.* **1991**, *17*, S137–S144. [[CrossRef](#)]

49. Vasenko, A.; Kirpichnikov, I.V.; Kuznetsov, V.A.; Starostin, A.S.; Dzhanian, A.G.; Markosian, G.E.; Oganessian, V.M.; Pogosov, V.S.; Tamanian, A.G.; Shakhazizian, S.R. New results in the ITEP/YePI double beta-decay experiment with enriched germanium detectors. *Mod. Phys. Lett. A* **1990**, *5*, 1299–1306. [[CrossRef](#)]
50. Balysh, A.; Beck, M.; Belyaev, S.T.; Bockholt, J.; Demehin, A.; Echternach, J.; Gurov, A.; Heusser, G.; Hirsch, M.; Klapdor-Kleingrothaus, H.V.; et al. The Heidelberg-Moscow double beta decay experiment with enriched  $^{76}\text{Ge}$ . First results. *Phys. Lett. B* **1992**, *283*, 32–36. [[CrossRef](#)]
51. Balysh, A.; Beck, M.; Belyaev, S.T.; Bockholt, J.; Demehin, A.; Gurov, A.; Hellmig, J.; Heusser, G.; Hirsch, M.; Hoffmann, C.; et al. Sub-eV limit for the neutrino mass from  $^{76}\text{Ge}$  double beta decay by the HEIDELBERG-MOSCOW experiment. *Phys. Lett. B* **1995**, *356*, 450–455. [[CrossRef](#)]
52. Günther, M.; Hellmig, J.; Heusser, G.; Hirsch, M.; Klapdor-Kleingrothaus, H.V.; Maier, B.; Päs, H.; Petry, F.; Ramachers, Y.; Strecker, H.; et al. Heidelberg-Moscow  $\beta\beta$  experiment with  $^{76}\text{Ge}$ : Full setup with five detectors. *Phys. Rev. D* **1997**, *55*, 54–67. [[CrossRef](#)]
53. Klapdor-Kleingrothaus, H.V.; Dietz, A.; Baudis, L.; Heusser, G.; Krivosheina, I.V.; Kolb, S.; Majorovits, B.; Paes, H.; Strecker, H.; Alexeev, V.; et al. Latest results from the Heidelberg-Moscow double beta decay experiment. *Eur. Phys. J.* **2001**, *A12*, 147–154. [[CrossRef](#)]
54. Bakalyarov, A.M.; Balysh, A.Y.; Belyaev, S.T.; Lebedev, V.I.; Zhukov, S.V. Results of the experiment on investigation of Germanium-76 double beta decay: Experimental data of Heidelberg-Moscow collaboration November 1995–August 2001. *Phys. Part Nucl. Lett.* **2005**, *2*, 77–81.
55. Aalseth, C.E.; Avignone, F.T.; Brodzinski, R.L.; Collar, J.I.; Garcia, E.; Gonzalez, D.; Hasenbalg, F.; Hensley, W.K.; Kirpichnikov, I.V.; Klimenko, A.A.; et al. Neutrinoless double- $\beta$  decay of  $^{76}\text{Ge}$ : First results from the International Germanium Experiment (IGEX) with six isotopically enriched detectors. *Phys. Rev. C* **1999**, *59*, 2108–2113. [[CrossRef](#)]
56. Aalseth, C.E.; Avignone, F.T.; Brodzinski, R.L.; Cebrian, S.; Garcia, E.; Gonzalez, D.; Hensley, W.K.; Irastorza, I.G.; Kirpichnikov, I.V.; Klimenko, A.A.; et al. The IGEX Ge-76 neutrinoless double beta decay experiment: Prospects for next generation experiments. *Phys. Rev. D* **2002**, *65*, 092007. [[CrossRef](#)]
57. Klapdor-Kleingrothaus, H.V.; Dietz, A.; Harney, H.L.; Krivosheina, I.V. Evidence for neutrinoless double beta decay. *Mod. Phys. Lett. A* **2001**, *16*, 2409–2420. [[CrossRef](#)]
58. Klapdor-Kleingrothaus, H.V.; Krivosheina, I.V.; Dietz, A.; Chkvorets, O. Search for neutrinoless double beta decay with enriched Ge-76 in Gran Sasso 1990–2003. *Phys. Lett.* **2004**, *B586*, 198–212. [[CrossRef](#)]
59. Klapdor-Kleingrothaus, H.V.; Krivosheina, I.V. The evidence for the observation of  $0\nu\beta\beta$  decay: The identification of  $0\nu\beta\beta$  events from the full spectra. *Mod. Phys. Lett. A* **2006**, *21*, 1547–1566. [[CrossRef](#)]
60. Schwingenheuer, B. Status and prospects of searches for neutrinoless double beta decay. *Ann. Phys.* **2013**, *525*, 269–280. [[CrossRef](#)]
61. Agostini, M.; Allardt, M.; Andreotti, E.; Bakalyarov, A.M.; Balata, M.; Barabanov, I.; Barnabé Heider, M.; Barros, N.; Baudis, L.; Bauer, C.; et al. Results on Neutrinoless Double- $\beta$  Decay of  $^{76}\text{Ge}$  from Phase I of the GERDA Experiment. *Phys. Rev. Lett.* **2013**, *111*, 122503. [[CrossRef](#)]
62. Agostini, M.; Allardt, M.; Bakalyarov, A.M.; Balata, M.; Barabanov, I.; Baudis, L.; Bauer, C.; Bellotti, E.; Belogurov, S.; Belyaev, S.T.; et al. Background free search for neutrinoless double beta decay with GERDA Phase II. *Nature* **2017**, *544*, 47. [[CrossRef](#)]
63. Agostini, M.; Bakalyarov, A.M.; Balata, M.; Barabanov, I.; Baudis, L.; Bauer, C.; Bellotti, E.; Belogurov, S.; Bettini, A.; Bezrukov, L.; et al. Improved Limit on Neutrinoless Double- $\beta$  Decay of  $^{76}\text{Ge}$  from GERDA Phase II. *Phys. Rev. Lett.* **2018**, *120*, 132503. [[CrossRef](#)]
64. Agostini, M.; Araujo, G.R.; Bakalyarov, A.M.; Balata, M.; Barabanov, I.; Baudis, L.; Bauer, C.; Bellotti, E.; Belogurov, S.; Bettini, A.; et al. Final Results of GERDA on the Search for Neutrinoless Double- $\beta$  Decay. *Phys. Rev. Lett.* **2020**, *125*, 252502. [[CrossRef](#)]
65. Aalseth, C.E.; Abgrall, N.; Aguayo, E.; Alvis, S.I.; Amman, M.; Arnquist, I.J.; Avignone, F.T.; Back, H.O.; Barabash, A.S.; Barbeau, P.S.; et al. Search for Neutrinoless Double- $\beta$  Decay in  $^{76}\text{Ge}$  with the Majorana Demonstrator. *Phys. Rev. Lett.* **2018**, *120*, 132502. [[CrossRef](#)]
66. Abgrall, N.; Abramov, A.; Abrosimov, N.; Abt, I.; Agostini, M.; Agartioglu, M.; Ajjaq, A.; Alvis, S.I.; Avignone, F.T.; Bai, X.; et al. The Large Enriched Germanium Experiment for Neutrinoless Double Beta Decay (LEGEND). *AIP Conf. Proc.* **2017**, *1894*, 020027. [[CrossRef](#)]
67. Ackermann, K.H.; Agostini, M.; Allardt, M.; Altmann, M.; Andreotti, E.; Bakalyarov, A.M.; Balata, M.; Barabanov, I.; Barnabé Heider, M.; Barros, N.; et al. The GERDA experiment for the search of  $0\nu\beta\beta$  decay in  $^{76}\text{Ge}$ . *Eur. Phys. J. C* **2013**, *73*, 2330. [[CrossRef](#)]
68. Agostini, M.; Bakalyarov, A.M.; Balata, M.; Barabanov, I.; Baudis, L.; Bauer, C.; Bellotti, E.; Belogurov, S.; Belyaev, S.T.; Benato, G.; et al. Upgrade for Phase II of the Gerda experiment. *Eur. Phys. J. C* **2018**, *78*, 388. [[CrossRef](#)]
69. Heusser, G. Low-radioactivity background techniques. *Ann. Rev. Nucl. Part Sci.* **1995**, *45*, 543–590. [[CrossRef](#)]
70. Agostini, M.; Bakalyarov, A.M.; Andreotti, E.; Balata, M.; Barabanov, I.; Baudis, L.; Barros, N.; Bauer, C.; Bellotti, E.; Belogurov, S.; et al. Characterization of 30  $^{76}\text{Ge}$  enriched Broad Energy Ge detectors for GERDA Phase II. *Eur. Phys. J. C* **2019**, *79*, 978. [[CrossRef](#)]
71. Cooper, R.; Radford, D.; Hausladen, P.; Lagergren, K. A novel HPGe detector for gamma-ray tracking and imaging. *Nucl. Instrum. Methods A* **2011**, *665*, 25–32. [[CrossRef](#)]

72. Agostini, M.; Araujo, G.; Bakalyarov, A.M.; Balata, M.; Barabanov, I.; Baudis, L.; Bauer, C.; Bellotti, E.; Belogurov, S.; Bettini, A.; et al. Characterization of inverted coaxial  $^{76}\text{Ge}$  detectors in GERDA for future double- $\beta$  decay experiments. *Eur. Phys. J. C* **2021**, *81*, 505. [[CrossRef](#)]
73. Freund, K.; Falkenstein, R.; Grabmayr, P.; Hegai, A.; Jochum, J.; Knapp, M.; Lubsandorzhiev, B.; Ritter, F.; Schmitt, C.; Schütz, A.-K.; et al. The Performance of the Muon Veto of the GERDA Experiment. *Eur. Phys. J. C* **2016**, *76*, 298. [[CrossRef](#)]
74. Barabanov, I.; Bezrukov, L.; Demidova, E.; Gurentsov, V.; Kianovsky, S.; Knopfle, K.T.; Kornoukhov, V.; Schwingenheuer, B.; Vasenko, A. Shielding of the GERDA experiment against external gamma background. *Nucl. Instrum. Methods A* **2009**, *606*, 790–794. [[CrossRef](#)]
75. Agostini, M.; Allardt, M.; Bakalyarov, A.M.; Balata, M.; Barabanov, I.; Barros, N.; Baudis, L.; Bauer, C.; Becerici-Schmidt, N.; Bellotti, E.; et al. Improvement of the energy resolution via an optimized digital signal processing in GERDA Phase I. *Eur. Phys. J. C* **2015**, *75*, 255. [[CrossRef](#)]
76. Agostini, M.; Allardt, M.; Andreotti, E.; Bakalyarov, A.M.; Balata, M.; Barabanov, I.; Barnabé Heider, M.; Barros, N.; Baudis, L.; Bauer, C.; et al. Pulse shape discrimination for GERDA Phase I data. *Eur. Phys. J. C* **2013**, *73*, 2583. [[CrossRef](#)]
77. Budjáš, D.; Barnabé Heider, M.; Chkvorets, O.; Khanbekov, N.; Schönert, S. Pulse shape discrimination studies with a Broad-Energy Germanium detector for signal identification and background suppression in the GERDA double beta decay experiment. *JINST* **2009**, *4*, P10007. [[CrossRef](#)]
78. Agostini, M.; Bakalyarov, A.M.; Balata, M.; Barabanov, I.; Baudis, L.; Bauer, C.; Bellotti, E.; Belogurov, S.; Bettini, A.; Bezrukov, L.; et al. First Search for Bosonic Superweakly Interacting Massive Particles with Masses up to  $1\text{ MeV}/c^2$  with GERDA. *Phys. Rev. Lett.* **2020**, *125*, 011801. [[CrossRef](#)] [[PubMed](#)]
79. Agostini, M.; Allardt, M.; Bakalyarov, A.M.; Balata, M.; Barabanov, I.; Barros, N.; Baudis, L.; Bauer, C.; Becerici-Schmidt, N.; Bellotti, E.; et al. Results on  $\beta\beta$  decay with emission of two neutrinos or Majorons in  $^{76}\text{Ge}$  from GERDA Phase I. *Eur. Phys. J. C* **2015**, *75*, 416. [[CrossRef](#)]
80. Agostini, M.; Allardt, M.; Bakalyarov, A.M.; Balata, M.; Barabanov, I.; Barros, N.; Baudis, L.; Bauer, C.; Becerici-Schmidt, N.; Bellotti, E.; et al.  $2\nu\beta\beta$  decay of  $^{76}\text{Ge}$  into excited states with GERDA Phase I. *J. Phys. G* **2015**, *42*, 115201. [[CrossRef](#)]
81. Abgrall, N.; Aguayo, E.; Avignone, F.T.; Barabash, A.S.; Bertrand, F.E.; Boswell, M.; Brudanin, V.; Busch, M.; Caldwell, A.S.; Chan, Y.-D.; et al. The Majorana Demonstrator Neutrinoless Double-Beta Decay Experiment. *Adv. High Energy Phys.* **2014**, *2014*, 365432. [[CrossRef](#)]
82. Luke, P.; Goulding, F.; Madden, N.; Pehl, R. Low capacitance large volume shaped-field germanium detector. *IEEE Trans. Nucl. Sci.* **1989**, *36*, 926–930. [[CrossRef](#)]
83. Barbeau, P.S.; Collar, J.I.; Tench, O. Large-mass ultralow noise germanium detectors: Performance and applications in neutrino and astroparticle physics. *J. Cosmol. Astropart. Phys.* **2007**, *2007*, 009. [[CrossRef](#)]
84. Abgrall, N.; Arnquist, I.J.; Avignone, F.T.; Barabash, A.S.; Bertrand, F.E.; Boswell, M.; Bradley, A.W.; Brudanin, V.; Busch, M.; Buuck, M.; et al. The Majorana Demonstrator calibration system. *Nucl. Instrum. Methods A* **2017**, *872*, 16–22. [[CrossRef](#)]
85. Guinn, I.; Arnquist, I.J.; Avignone, F.T.; Barabash, A.S.; Barton, C.J.; Bertrand, F.E.; Bos, B.; Busch, M.; Buuck, M.; Caldwell, T.S.; et al. Results of the Majorana Demonstrator’s Search for Double-Beta Decay of  $^{76}\text{Ge}$  to Excited States of  $^{76}\text{Se}$ . *J. Phys. Conf. Ser.* **2020**, *1468*, 012115. [[CrossRef](#)]
86. Guinn, I.; Abgrall, N.; Avignone, F.T.; Barabash, A.S.; Bertrand, F.E.; Brudanin, V.; Busch, M.; Buuck, M.; Byram, D.; Caldwell, A.S.; et al. Low Background Signal Readout Electronics for the Majorana Demonstrator. *J. Phys. Conf. Ser.* **2015**, *606*, 012009. [[CrossRef](#)]
87. Abgrall, N.; Allmond, J.M.; Arnquist, I.J.; Avignone, F.T.; Barabash, A.S.; Barton, C.J.; Bertrand, F.E.; Bos, B.; Busch, M.; Buuck, M.; et al. ADC Nonlinearity Correction for the Majorana Demonstrator. *IEEE Trans. Nucl. Sci.* **2021**, *68*, 359–367. [[CrossRef](#)]
88. Vetter, K.; Kuhn, A.; Lee, I.Y.; Clark, R.; Cromaz, M.; Deleplanque, M.; Diamond, R.; Fallon, P.; Lane, G.; Macchiavelli, A.; et al. Performance of the GRETA prototype detectors. *Nucl. Instrum. Methods Phys. Res. Sect. A* **2000**, *452*, 105–114. [[CrossRef](#)]
89. Fano, U. Ionization Yield of Radiations. II. The Fluctuations of the Number of Ions. *Phys. Rev.* **1947**, *72*, 26–29. [[CrossRef](#)]
90. Alvis, S.I.; Arnquist, I.J.; Avignone, F.T.; Barabash, A.S.; Barton, C.J.; Basu, V.; Bertrand, F.E.; Bos, B.; Buuck, M.; Caldwell, T.S.; et al. Multisite event discrimination for the Majorana Demonstrator. *Phys. Rev. C* **2019**, *99*, 065501. [[CrossRef](#)]
91. Boswell, M.; Chan, Y.-D.; Detwiler, J.; Finnerty, P.; Henning, R.; Gehman, V.; Johnson, R.A.; Jordan, D.V.; Kazkaz, K.; Knapp, M.; et al. MaGe—a Geant4-Based Monte Carlo Application Framework for Low-Background Germanium Experiments. *IEEE Trans. Nucl. Sci.* **2011**, *58*, 1212–1220. [[CrossRef](#)]
92. Agostinelli, S.; Allison, J.; Amako, K.; Apostolakis, J.; Araujo, H.; Arce, P.; Asai, M.; Axen, D.; Banerjee, S.; Barrand, G.; et al. GEANT4—A simulation toolkit. *Nucl. Instrum. Methods A* **2003**, *506*, 250–303. [[CrossRef](#)]
93. Feldman, G.J.; Cousins, R.D. Unified approach to the classical statistical analysis of small signals. *Phys. Rev. D* **1998**, *57*, 3873–3889. [[CrossRef](#)]
94. Verkerke, W.; Kirkby, D.P. The RooFit toolkit for data modeling. *arXiv* **2003**, arXiv:physics/0306116.
95. Schott, G. RooStats for Searches. In *PHYSTAT 2011*; CERN: Geneva, Switzerland, 2011. [[CrossRef](#)]
96. Horoi, M.; Neacsu, A. Shell model predictions for  $^{124}\text{Sn}$  double- $\beta$  decay. *Phys. Rev. C* **2016**, *93*, 024308. [[CrossRef](#)]
97. Hyvärinen, J.; Suhonen, J. Nuclear matrix elements for  $0\nu\beta\beta$  decays with light or heavy Majorana-neutrino exchange. *Phys. Rev. C* **2015**, *91*, 024613. [[CrossRef](#)]

98. López Vaquero, N.; Rodríguez, T.R.; Egado, J.L. Shape and pairing fluctuations effects on neutrinoless double beta decay nuclear matrix elements. *Phys. Rev. Lett.* **2013**, *111*, 142501. [[CrossRef](#)]
99. Yao, J.M.; Song, L.S.; Hagino, K.; Ring, P.; Meng, J. Systematic study of nuclear matrix elements in neutrinoless double- $\beta$  decay with a beyond-mean-field covariant density functional theory. *Phys. Rev. C* **2015**, *91*, 024316. [[CrossRef](#)]
100. Mirea, M.; Pahomi, T.; Stoica, S. Values of the phase space factors involved in double beta decay. *Rom. Rep. Phys.* **2015**, *67*, 872.
101. LEGEND Collaboration. The Large Enriched Germanium Experiment for Neutrinoless  $\beta\beta$  decay, LEGEND-1000 Pre-Conceptual Design Report. Unpublished work, 2021.
102. Domula, A.; Hult, M.; Kermaidic, Y.; Marissens, G.; Schwingenheuer, B.; Wester, T.; Zuber, K. Pulse shape discrimination performance of inverted coaxial Ge detectors. *Nucl. Instrum. Methods A* **2018**, *891*, 106–110. [[CrossRef](#)]
103. Abgrall, N.; Aguayo, E.; Avignone, F.T.; Barabash, A.S.; Bertrand, F.E.; Boswell, M.; Brudanin, V.; Busch, M.; Byram, D.; Caldwell, A.S.; et al. The Majorana Low-noise Low-background Front-end Electronics. *Phys. Procedia* **2015**, *61*, 654–657. [[CrossRef](#)]
104. Riboldi, S.; Pullia, A.; Cattadori, C. Improvement of the “CC2” charge sensitive preamplifier for the GERDA phase II experiment. In Proceedings of the 2012 IEEE Nuclear Science Symposium and Medical Imaging Conference and 19th Workshop on Room-Temperature Semiconductor X-ray and Gamma-ray Detectors, Anaheim, CA, USA, 27 October–3 November 2012. [[CrossRef](#)]
105. Willers, M. Signal Readout Electronics for LEGEND-200. *J. Phys. Conf. Ser.* **2020**, *1468*, 012113. [[CrossRef](#)]
106. Abgrall, N.; Arnquist, I.J.; Avignone, F.T.; Back, H.O.; Barabash, A.S.; Bertrand, F.; Boswell, M.; Bradley, A.W.; Brudanin, V.; Busch, M.; et al. The Majorana Demonstrator radioassay program. *Nucl. Instrum. Methods A* **2016**, *828*, 22–36. [[CrossRef](#)]
107. Myslik, J. LEGEND: The Large Enriched Germanium Experiment for Neutrinoless Double-Beta Decay. In Proceedings of the 13th Conference on the Intersections of Particle and Nuclear Physics, Palm Springs, CA, USA, 29 May–3 June 2018.
108. Efremenko, Y.; Fajt, L.; Hodák, R.; Štekl, I.; Febbraro, M.; Radford, D.; Fischer, F.; Hayward, C.; Kraetzschmar, T.; Majorovits, B.; et al. Use of poly(ethylene naphthalate) as a self-vetoing structural material. *JINST* **2019**, *14*, P07006. [[CrossRef](#)]
109. Manzanillas, L.; Abt, I.; Efremenko, Y.; Febbraro, M.; Fischer, F.; Guitart, M.; Gusev, K.; Hackett, B.; Hayward, C.; Hodák, R.; et al. Usage of PEN as self-vetoing structural material in low background experiments. *arXiv* **2020**, arXiv:2011.08983. [[CrossRef](#)]
110. Zsigmond, A.J. et al. [LEGEND Collaboration]. LEGEND: The future of neutrinoless double-beta decay search with germanium detectors. *J. Phys. Conf. Ser.* **2020**, *1468*, 012111. [[CrossRef](#)]
111. Edzards, F. et al. [LEGEND Collaboration]. The Future of Neutrinoless Double Beta Decay Searches with Germanium Detectors. *J. Phys. Conf. Ser.* **2020**, *1690*, 012180. [[CrossRef](#)]